FINAL REPORT

A Low Frequency Electromagnetic Sensor for Underwater Geo-Location

SERDP Project MR-1719

MAY 2011

Dr. Fridon Shubitidze
Sky Research, Inc

This document has been cleared for public release

SERDP
DOD ▪ EPA ▪ DOE

Report Documentation Page

Form Approved
OMB No. 0704-0188

Public reporting burden for the collection of information is estimated to average 1 hour per response, including the time for reviewing instructions, searching existing data sources, gathering and maintaining the data needed, and completing and reviewing the collection of information. Send comments regarding this burden estimate or any other aspect of this collection of information, including suggestions for reducing this burden, to Washington Headquarters Services, Directorate for Information Operations and Reports, 1215 Jefferson Davis Highway, Suite 1204, Arlington VA 22202-4302. Respondents should be aware that notwithstanding any other provision of law, no person shall be subject to a penalty for failing to comply with a collection of information if it does not display a currently valid OMB control number.

1. REPORT DATE	2. REPORT TYPE	3. DATES COVERED
MAY 2011	**N/A**	**-**

4. TITLE AND SUBTITLE	5a. CONTRACT NUMBER
A Low Frequency Electromagnetic Sensor for Underwater Geo-Location	5b. GRANT NUMBER
	5c. PROGRAM ELEMENT NUMBER
6. AUTHOR(S)	5d. PROJECT NUMBER
	5e. TASK NUMBER
	5f. WORK UNIT NUMBER
7. PERFORMING ORGANIZATION NAME(S) AND ADDRESS(ES) **Sky Research, Inc**	8. PERFORMING ORGANIZATION REPORT NUMBER
9. SPONSORING/MONITORING AGENCY NAME(S) AND ADDRESS(ES)	10. SPONSOR/MONITOR'S ACRONYM(S)
	11. SPONSOR/MONITOR'S REPORT NUMBER(S)

12. DISTRIBUTION/AVAILABILITY STATEMENT
Approved for public release, distribution unlimited

13. SUPPLEMENTARY NOTES
The original document contains color images.

14. ABSTRACT

The research described in this report was conducted in fulfillment of Project MM- 1719, A Low Frequency Electromagnetic Sensor for Underwater Geo-Location, submitted to the Strategic Environmental Research and Development Programs (SERDP) Exploratory Development Program (SEED) in response to Statement of Need MMSEED-10-01, Advanced Technologies for Detection, Discrimination, and Remediation of Military Munitions on Land and Underwater. The main focus of this research was to explore and develop a new low frequency Electromagnetic Sensor modality for fast and accurate Geo-Location that would be based on the measured vector magnetic field, which would be sufficiently robust and efficient to be used in the real field for underwater UXO detection and discrimination systems tracking and positioning. In this project we concentrated on the fundamental mathematical, physical, computer simulation and potential practical implementations aspects of the proposed approaches. The report provides both the mathematical fundamentals and physical meanings of the proposed approach for underwater geolocation. Namely we explore two techniques for underwater geo-location using low frequency magnetic field: a) the first technique was based on the vector magnetic field full tensor gradient estimations at a given point, b) the second uses the non-linear optimization algorithm based on the differential evolution (DE) approach. We studied the sensitivity of the vector magnetic field gradient estimations using the standard finite different approach. In addition we utilized the three dimensional EMI solver based on the method of auxiliary sources for estimating the noise due to a spherical and spheroidal UXO like targets. We studied the accuracy with which the system can estimate a transmitters location, their robustness with respect to noise, and their requirements with regard to data quality and quantity.

15. SUBJECT TERMS

16. SECURITY CLASSIFICATION OF:			17. LIMITATION OF ABSTRACT	18. NUMBER OF PAGES	19a. NAME OF RESPONSIBLE PERSON
a. REPORT **unclassified**	b. ABSTRACT **unclassified**	c. THIS PAGE **unclassified**	**SAR**	**78**	

Standard Form 298 (Rev. 8-98)
Prescribed by ANSI Std Z39-18

This report was prepared under contract to the Department of Defense Strategic Environmental Research and Development Program (SERDP). The publication of this report does not indicate endorsement by the Department of Defense, nor should the contents be construed as reflecting the official policy or position of the Department of Defense. Reference herein to any specific commercial product, process, or service by trade name, trademark, manufacturer, or otherwise, does not necessarily constitute or imply its endorsement, recommendation, or favoring by the Department of Defense.

ABSTRACT

The research described in this report was conducted in fulfillment of Project MM-1719, "A Low Frequency Electromagnetic Sensor for Underwater Geo-Location," submitted to the Strategic Environmental Research and Development Program's (SERDP) Exploratory Development Program (SEED) in response to Statement of Need MMSEED-10-01, "Advanced Technologies for Detection, Discrimination, and Remediation of Military Munitions on Land and Underwater."

The main focus of this research was to explore and develop a new low frequency Electromagnetic Sensor modality for fast and accurate Geo-Location that would be based on the measured vector magnetic field, which would be sufficiently robust and efficient to be used in the real field for underwater UXO detection and discrimination systems tracking and positioning. In this project we concentrated on the fundamental mathematical, physical, computer simulation and potential practical implementations aspects of the proposed approaches. The report provides both the mathematical fundamentals and physical meanings of the proposed approach for underwater geo-location. Namely we explore two techniques for underwater geo-location using low frequency magnetic field: a) the first technique was based on the vector magnetic field full tensor gradient estimations at a given point, b) the second uses the non-linear optimization algorithm based on the differential evolution (DE) approach. We studied the sensitivity of the vector magnetic field gradient estimations using the standard finite different approach. In addition we utilized the three dimensional EMI solver based on the method of auxiliary sources for estimating the noise due to a spherical and spheroidal UXO like targets. We studied the accuracy with which the system can estimate a transmitter's location, their robustness with respect to noise, and their requirements with regard to data quality and quantity.

We illustrated that both vector magnetic field full tensor gradient and DE techniques have the potential to provide centimeter-level underwater geo-location. However, when the primary magnetic field signals are contaminated with random noise due to underwater metallic targets, water conductivity/frequency changes, and transmitter size, the performance of the vector magnetic field full tensor gradient approach degrades significantly compared to that of the non-linear DE optimization technique. In addition, the number of receivers (Rx) required by the vector magnetic field tensor gradient technique and its sensitivity with respect to sensor separations prevented us from further considering this technique for UW geo-location, leaving the non-linear approach that uses only three vector Rx as our technique of choice for tracking the location of underwater interrogation sensors with centimeter-level accuracy.

As part of this investigation we developed an experimental system to evaluate the effects of sensor noise/sensitivity on localization accuracy. The experimental setup comprises a large moment dipole transmitter, a current source, and a magnetic field gradient receiver array. Highest quality gradient estimates were achieved with three vector magnetometers equally spaced and aligned with each axis (centered difference measurement). The data were collected outdoor at Sky Research Hanover, Office. The new proposed approach was applied to these data and the transmitter coil's locations were determined with reasonable accuracy.

ACKNOWLEDGMENTS

The Principal Investigator, Dr. Fridon Shubitidze of Sky Research conceived, implemented, and tested most of the approaches presented in this report. He developed the vector magnetic field full tensor gradient and deferential evolution approaches and integrated them into a location algorithm that can be implemented to UW sensor geo-location system using the magnetic field.

Mrs. Irma Shamatava of Sky Research, who is an expert in the MAS, conducted detailed EMI noise estimation studies.

Mr. Jon Miller built an experimental prototype system, collected the magnetic data, and conducted data analysis and verified the theoretical approaches using the actual data.

Mrs. Joy Rogalla edited successive drafts of this report.

Funding for this project was provided by the Strategic Environmental Research and Development Program Office. We wish to express our sincere appreciation to Dr. Jeffrey Marqusee, Dr. Anne Andrews, Dr. Herb Nelson, and staff of the SERDP Office for providing support and funding for this project.

This report was prepared under contract to the Department of Defense Strategic Environmental Research and Development Program. The publication of this report does not indicate endorsement by the Department of Defense, nor should the contents be construed as reflecting the official policy or position of the Department of Defense. Reference herein to any specific commercial product, process, or service by trade name, trademark, manufacturer, or otherwise, does not necessarily constitute or imply its endorsement, recommendation, or favoring by the Department of Defense.

TABLE OF CONTENTS

LIST OF FIGURES

LIST OF TABLES

LIST OF ACRONYMS

A-m^2	Ampere-meter-squared
BEM	Boundary Element Method
cm	Centimeter
DC	Direct Current
DE	Differential Evolution
DVL	Doppler Velocity Log
EMI	Electromagnetic Induction
FEM	Finite Element Method
GPS	Global Positioning System
HAP	Magnetic Field (**H),** Magnetic Field Vector (**A)** and Scalar (**P**) Potentials
Hz	Hertz
LBL	Long Baseline
LC	L-inductance, C-capacitance
m	Meter
mm	Millimeter
MAS	Method of Auxiliary Sources
MPV-TD	Man-portable Vector Time Domain
MQS	Magneto Quasi-Static
nT	nanoTesla
RF	Radio Frequency
Rx	Receiver
S/m	Siemens/meter
SEED	SERDP Exploratory Development Program
SERDP	Strategic Environmental Research and Development Program
SIBC	Surface Impedance Boundary Condition
SNR	Signal-to-noise Ratio
Tx	Transmitter
USACE	U.S. Army Corps of Engineers
UUV	Unmanned Underwater Vehicle
UW	Underwater
UXO	Unexploded Ordnance

1 INTRODUCTION

1.1 Background and objectives

The research described in this report was conducted in fulfillment of Project MM-1719, "A Low Frequency Electromagnetic Sensor for Underwater Geo-Location," under the Strategic Environmental Research and Development Program's (SERDP) Exploratory Development Program (SEED) in response to Statement of Need MMSEED-10-01, "Advanced Technologies for Detection, Discrimination, and Remediation of Military Munitions on Land and Underwater."

Detecting and discriminating Unexploded Ordnance (UXO) in the underwater (UW) environment presents additional challenges relative to that in terrestrial environments. In particular, UW sites contain large amounts of environmental clutter, debris, and obstacles, such as pilings, crab pots, anchors, coral, and trash [1]-[8]. The high conductivity of sea water severely limits the efficacy of geo-location systems that employ radio frequency (RF) transmission (e.g., global positioning systems [GPS]). Optical location methods, such as laser triangulation, are also inhibited by attenuation in UW environments. In terrestrial applications, electromagnetic induction (EMI) responses are recorded, and then processing techniques are applied to well-controlled magnetic and EMI data sets. Subsequently, target parameters, such as the dipole polarizability tensor, time decay rate, and associated object size, shape and orientation are estimated to discriminate munitions from clutter or geology. Terrestrial UXO discrimination studies have demonstrated that poor transmitter/receiver sensor location accuracy (worse than 5-10 centimeters [cm]) significantly reduces the ability to extract meaningful discrimination parameters from data. Usually underwater sites, because of the dynamic nature and unfavorable RF propagation characteristics, are more complex and challenging than terrestrial sites; therefore even with current technologies it is very difficult to obtain the desired centimeter-level position accuracy to support advanced discrimination processing techniques using magnetic and EM data. Moreover, positioning in the underwater environment relies heavily on our ability to accurately measure the geometry of a towed array or periodic GPS re-acquisition by unmanned underwater vehicles (UUVs) – both of which lead to the propagation of positional errors in survey data. Thus, to enhance UW munitions detection and reliable ordnance discrimination and to reduce remediation costs of UW UXO cleanup [5], new geo-location sensors with centimeter-level position accuracy and sufficient signal-to-noise ratio (SNR) are needed.

To achieve this goal, in this work we investigated a new UW Geo-location system's performance in the UW environment. The new system utilizes measurements of a pulsed direct current (DC) magnetic field and its tensor gradients at a given spatial point (see Figure 1). The magnetic field is measured using tri-axial sensor configurations. The theoretical basis of the proposed approach is the magnetic field vector gradient and is founded on the magnetic field **H,** magnetic field vector **A** and scalar P potentials (HAP). The original proposed system consists of a magnetic dipole field transmitter, that is placed on the sea surface and geo-referenced with a GPS, and a magnetic positioning system coupled to an underwater detection/interrogation system and geo-referenced with respect to the transmitter (Tx) coil. The magnetic positioning system has five tri-axial magnetic sensors that record the field generated from the magnetic dipole transmitter. The dipole transmitter produces a pulsed signal that the receivers record in the

positioning system continuously. The background field is subtracted by taking differences between the magnetic field measurements recorded during "on" and "off" times the. This technique enables measurement of the vector field and tensor gradient generated by the transmitter at a given point, and in return it allows precise calculation of the detection system position relative to the transmitter.

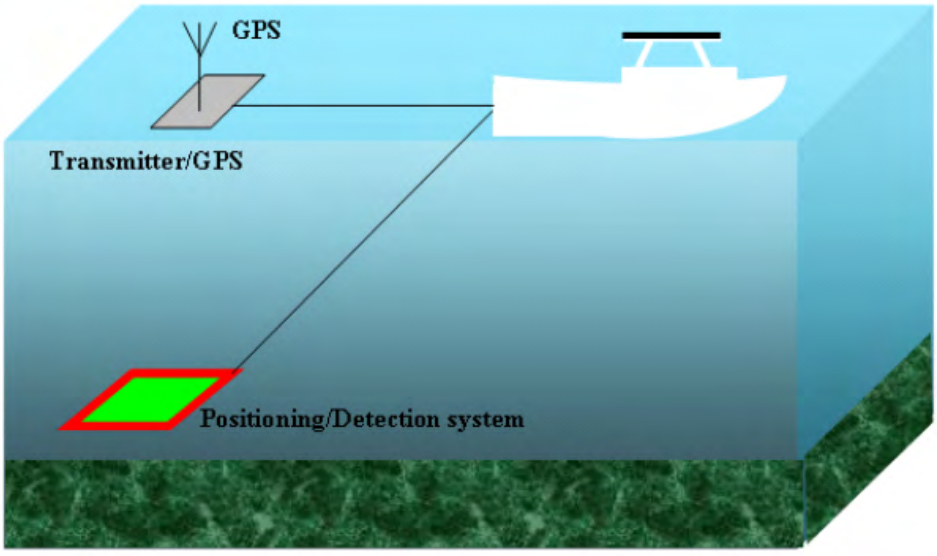

Figure 1. Schematic diagram of the proposed system. Both the magnetic positioning and transmitter systems will be towed on a boat. The magnetic positioning system will track the detection system's location relative to the geo-referenced transmitter.

The primary objective of this project was to investigate the proposed new system's performance in the UW environment using computational tools and to build and conduct measurements in controlled environments. Specifically, the objectives were to:

- Systematically investigate what configuration of an active DC magnetic field transmitter offers the optimal compromise between size, shape and practical implementation for the maximum transmitter range in UW environments for locating the transmitter with centimeter-level accuracy.
- Optimize and design tri-axial receiver sensors configurations to accurately approximate the tensor gradient of an actively transmitted DC magnetic field from the *spatial differences* between the receivers. The transmitted magnetic field and its gradient at the receiver locations will provide sufficient data for locating and tracking underwater UXO sensors with respect to the surface GPS system.
- Systematically investigate how noise, such as the air-water interface, will influence the proposed system performance and establish the transmitter's location precision and accuracy baseline under the commonly encountered noise levels. All basic UW EMI phenomena were investigated using the three dimensional EMI solver called the method of auxiliary sources (MAS).

The MAS is a numerical technique, originally designed for solving various electromagnetic radiation and scattering problems. MAS is a robust, easy to implement, and accurate method for studying a wide range of electromagnetic problems, such as the investigation of waveguide structures, antennas, scattering, electromagnetic wave propagation in complex media, etc. MAS has also been used successfully for the analysis of low frequency electromagnetic induction scattering phenomena [9]-[11]. Boundary value problems are solved numerically by representing the electromagnetic fields in each domain of the structure under investigation by a finite linear combination of analytical solutions of the relevant field equations corresponding to sources situated at some distance away from the boundaries of each domain. The "auxiliary sources" producing these analytical solutions are chosen to be elementary currents/charges located on fictitious auxiliary surface(s), usually conforming to the actual surface(s) of the structure. The method only requires points on the auxiliary and actual surfaces, without resorting to the detailed mesh structures as required by other methods (finite element method (FEM), boundary element method (BEM) etc).

1.2 Report structure

Chapter 2 outlines the theoretical bases of the technique for estimating the location of an underwater detection/interrogation system, coupled with a magnetic positioning system. This approach utilizes the vector magnetic field full tensor gradient. The tensor gradient is estimated using the measured vector magnetic field at least five or seven positions. As we shall see, the algorithm provides fast and accurate estimates of the UW system's location at least at fifteen meter (m) depths using low frequency, less than 100 Hertz (Hz) magnetic field. We also introduced an equivalent but more noise tolerant approach that uses a standard location estimation algorithm with the measured magnetic field at three locations. We also provide a brief description of the MAS technique for UW environments, which is used here for estimating the noise due to air/water interface and UXO-like metallic targets.

Chapter 3 illustrates numerical results, namely EMI signal sensitivity with respect to the frequency, and demonstration of transmitter size and observation distances. We show the comparisons between the analytical and finite difference derivatives. We systematically investigated noise due to permeable UW targets, the air-water interface and surface roughness, and those results are described. We explored two techniques for underwater geo-location using a low frequency magnetic field: a) first technique was based on the vector magnetic field full tensor gradient estimations at a given point, b) the second uses the non-linear optimization algorithm based on the differential evolution (DE) approach. We studied the accuracy with which the approach can estimate a transmitter's location, their robustness with respect to noise, and their requirements with regard to data quality and quantity. We ultimately wanted to determine which of vector magnetic field receiver sensors configurations would be practical and reliable for use in real underwater Geo-location for improving UXO detection and discrimination in conducting environment. We assessed the ability of each technique to predict the location of an underwater interrogation system by comparing estimated results to the ground truth. The studies were done for different water conductivities, Tx geometry, operating frequencies and additive random noises. We found that for realistic water conductivities, the frequency should be less than 100 Hz. This is due to the EM absorption in a conducting medium. In addition, our

studies showed that as the medium's conductivity increases the proposed system's performance degrades. This problem could overcome by lowering the frequency.

We illustrated that both the vector magnetic field full tensor gradient and DE techniques have the potential to provide centimeter-level underwater geo-location. However, when the primary magnetic field signals are contaminated with random noise that due to underwater metallic targets, water conductivity/frequency changes, and transmitter size, the performance of the vector magnetic field full tensor gradient approach degrades significantly compared to that of the non-linear DE optimization technique. In addition, the number of Rx required by the vector magnetic field tensor gradient technique and its sensitivity with respect to sensor separations prevented us from further considering this technique for UW geo-location, leaving the non-linear approach, that uses only three vector Rx, as our technique of choice for tracking the location of underwater interrogation sensors with centimeter-level accuracy.The DE tolerance to noise makes this approach our definitive candidate for UW geo-location.

Chapter 4 describes the experimental setup that we developed to evaluate the effects of sensor noise/sensitivity on localization accuracy. The experimental setup comprises a large moment dipole transmitter, a current source, and a magnetic field gradient receiver array. Highest quality gradient estimates are achieved with three vector magnetometers equally spaced and aligned with each axis (centered difference measurement). A minimum of 5 vector field measurements is required to estimate the complete magnetic field gradient tensor (centered difference along two orthogonal axes). The transmitter current source produces a 50% duty cycle waveform at frequencies ranging from sub-Hertz to several kHz. We determined the source field value at each receiver location by examining the difference in overall field strength during the on-time and off-time periods. This time difference method eliminates much of the background signal and reduces the effects of nearby ferrous objects or other noise sources. Available hardware limited our receiver array to a 10 Hz sample rate, which required a transmitter frequency below 1 Hz. It is expected that a prototype system would incorporate high bandwidth magnetometers capable of sampling the source field at 1 kHz or more. Higher bandwidth sensors would enable greater transmitter frequencies and shorter sample times to produce each localization measurement. It is anticipated that localization values could be produced at 5-10 Hz with high bandwidth receivers.

Finally, Chapter 5 summarizes the results and suggests future research directions.

2 THEORETICAL BASIS FOR GEO-LOCATING UW INTERROGATION SYSTEMS USING A LOW FREQUENCY MAGNETIC FIELD

2.1 Theory introduction

Subsurface marine sensor positioning is generally conducted using: (1) GPS positioning and geometric translation; (2) inertial navigation; (3) dead reckoning; (4) acoustic navigation; or a combination of them. Each approach defines a relative position that must be integrated with GPS to establish absolute location. GPS and simple geometric translation is often used for towed systems and incurs errors that increase with offset between the GPS and sensor locations. Dead reckoning is accomplished by measuring heading using a heading sensor (flux gate or fiber-optic gyro) and speed through the water using a water speed sensor like a Doppler velocity log (DVL) instrument. The positional accuracy degrades depending on the method employed. Long-baseline (LBL) acoustic methods create an accurate local reference frame for positioning but suffer from acoustic multi-path and attenuation in shallow or cluttered environments. Because of the dynamic nature of the highly variable UW environment, it is desirable to develop more accurate and reliable sensor positioning that will enable real-time processing and enhance classification approaches [1]-[9].

To achieve this goal, under this project we investigated a new UW Geo-location system. The system utilizes measurements of a pulsed DC vector magnetic field and its tensor gradients at a given spatial point. The magnetic field is measured using tri-axial sensor configurations. The theoretical basis of the proposed approach is founded on the further extension of the HAP method, developed under the SERDP-SEED MM-1592 project. The system contains a magnetic dipole field transmitter placed on the sea surface and geo-referenced with a GPS; and a magnetic positioning system coupled to an underwater detection/interrogation system. The magnetic positioning system has five tri-axial magnetic sensors that record the field generated from the magnetic dipole transmitter. The dipole transmitter produces a pulsed signal that the receivers in the positioning system records continuously. By taking differences between the magnetic field measurements recorded during “on” and “off” times, the system isolates a DC signal from the transmitter (i.e., by subtracting the background field). This approach enables measurement of the vector field and tensor gradient generated by the transmitter at a given point, allowing precise calculation of the detection system position relative to the transmitter. In addition we employed the non-linear optimization algorithm based on the DE approach to determine geo-location in non-dipole field region.

In this chapter, a brief description of the mathematical bases is presented for determining the underwater interrogation system’s location, and the MAS is described for the UW environment. The sensor tracking algorithm assumes that the transmitter is a magnetic dipolar source; it requires the measured magnetic field vector H at seven locations. After reviewing the

theoretical basis of the proposed closed for solution using the magnetic field vector gradient tensor approach, then mathematical expressions are given for a direct search approach.

2.2 A closed form solution for estimating a magnetic dipole location using a low frequency magnetic field

Recently, several methods for magnetic dipole localization have been proposed [13]. For example, Mcfee *et al.* [16] proposed to measure the magnetic field in a two-dimensional grid and perform a nonlinear least-squares fit to the data. Hashi *et al.* [22] localized an LC magnetic marker with a resonant frequency of 175 kHz. They measured the magnetic field distribution by a pickup coil array that consists of 25 coils placed at interval of 45 millimeters (mm) and determined the dipole parameters by the Gauss–Newton method. Yabukami *et al.* [18] measured the magnetic field by two three-axial fluxgate sensors and used the Powell method for estimating the position and the orientation of a magnetic dipole. They also localized two markers simultaneously using four sensors. Figure 2 presents the geometry of the dipole localization problem.

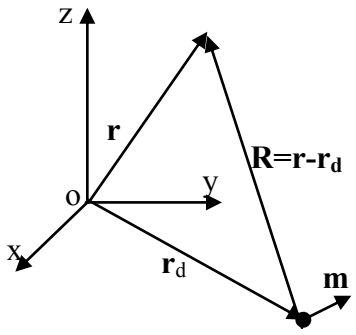

Figure 2. Geometry of the problem. A magnetic dipole located at $\mathbf{r}_d$.

Suppose that a magnetic dipole is placed at $\mathbf{r}_d$ position and has **m** magnetic dipole moment. Let **r** be position where a magnetic vector field sensor is placed. Then the magnetic field **H** and the scalar and vector potentials ψ and **A** at **r** point are:

$$\mathbf{H} = \frac{e^{jkR}}{4\pi R^3} \left(\left(\frac{3}{R^2} + \frac{3jk}{R} - k^2 \right) (\mathbf{R} \cdot \mathbf{m}) \right), \qquad (2.1)$$

$$\psi = \frac{(\mathbf{R}\cdot\mathbf{m})}{4\pi R^3}\ 1 - jkR\ \ e^{jkR}, \tag{2.2}$$

$$\mathbf{A} = \mu_o \frac{(\mathbf{m}\times\mathbf{R})}{4\pi R^3}\ 1 - jkR\ \ e^{jkR}, \tag{2.3}$$

where k is the wave number in the surrounding medium, $\mathbf{R} = \mathbf{r} - \mathbf{r}_d$, and the vectors $\mathbf{r}$ and $\mathbf{r}_d$ are the observation point and the location of the transmitter, which we assume to be a dipole (Stratton, 1941, Chapter 8) (see Figure 2). From (2.1) note that, in the electromagnetic wave regime, the magnetic field due to a magnetic dipole has terms that decay as R^{-1}, R^{-2}, and R^{-3}. The range $kR \gg 1$ is referred to as the far zone, and fields in this range are referred to as being in the far field. Similarly, fields in the near zone (with $kR \ll 1$) are referred to as being in the near field, while the zone $kR \approx 1$ is called the intermediate zone. This research is focused on the low frequency < 10 kHz EMI positioning system. Typically, UW interrogation sensor system location is conducted in the near and intermediate zones. Additionally, in the EMI regime, displacement currents are considered irrelevant, which means that the contribution of the k^2 term in (2.1) can be set to be zero. Under these assumptions we can take the dot product of (2.1) and **R** and use (2.2) to show that:

$$\mathbf{H} \left(\frac{1}{R^3} \right) \quad 2\frac{\mathbf{R}\ \mathbf{m}}{R^3} G(R,k) \quad 2 \quad , \tag{2.4}$$

where $G(R,k) = \ 1 - jkR\ \ e^{jkR} / 4\pi$.

Similarly, we can take the *cross* product of (2.1)and **R** and use (2.3) to obtain:

$$\mathbf{H} \left(\frac{1}{R^3} \right) \mathbf{R} \quad G(\mathrm{R,k}) \frac{\mathbf{m}\ \ \mathbf{R}}{R^3} \quad \frac{\mathbf{A}}{\mu_o}. \tag{2.5}$$

Now, taking the cross product of **H** and (2.5) gives:

$$\left[\mathbf{H} \left(\frac{\ }{\mu_o} \right) \right] \quad \mathbf{R}\ |\mathbf{H}|^2 \quad 2\mathbf{H} \quad \mathbf{R}\ |\mathbf{H}|^2, \tag{2.6}$$

and from this we can solve for **R**:

$$\mathbf{R} = \frac{2\mathbf{H}\,\psi + \mathbf{H}\times\mathbf{A}/\mu_o}{|\mathbf{H}|^2}. \tag{2.7}$$

Thus if we assume that the source is a single dipole we can express its location vector **R** in terms of only three global values. Moreover, this expression is independent of the frequency, which means that (2.7) is valid for both free space and conducting media such as water as long as the magneto quasi static (MQS) assumption holds; *i.e.,* as long as we can neglect displacement currents. Note that **R** is determined as a ratio between the three global values. This makes the expression in (2.7) partially tolerant to noise due to scaling arguments, since **A** and ψ depend on the **H** field (*cf.* (2.4) and (2.5)).

2.3 A closed-form expression for magnetic dipole localization by measurement of its magnetic field

The analytic expression (2.7) derived in the previous section requires the magnetic field vector **H**, the vector potential **A**, and the scalar magnetic potential ψ at a single location in space; the method uses seven global values to estimate the object's location, which, as we can see from(2.7), consists of only three unknown parameters. We now present a reduced HAP formulation that uses only the magnetic field and the scalar potential, thus decreasing the number of required global values and reducing computational requirements. Recalling that $\mathbf{R} = \mathbf{r} - \mathbf{r}_d$, where **r** and $\mathbf{r}_d$ are respectively the observation point and the dipole location in the global coordinate system (seeFigure 2), we can write (2.4) as:

$$\mathbf{H}\cdot(\mathbf{r}-\mathbf{r}_d) = 2\psi \tag{2.8}$$

or

$$\mathbf{H}\cdot\mathbf{r}_d = -2\psi + \mathbf{H}\cdot\mathbf{r}\ . \tag{2.9}$$

After taking the gradient of equation (2.9) with respect to the x-, y-, and z-coordinates, we have:

$$\begin{cases} x_d - [redacted] - y\frac{}{x} - z\frac{H_z}{x} \\ x_d - [redacted] - y\frac{}{y} - z\frac{H_z}{y} \\ x_d - [redacted] - y\frac{}{z} - z\frac{H_z}{z} \end{cases}. \tag{2.10}$$

Thus, in order to determine the transmitter's location we need only the magnetic field **H** and its gradient at a given point in space.

2.4 Estimating the magnetic field's tensor gradient

2.4.1 Seven vector receivers approach

The closed form approach (2.10) requires the gradient of the vector magnetic field along all three x, y and z directions. The current state of the art sensors, such as the MetalMapper and Man Portable Vector Time Domain (MPV-TD) system, have the ability to accurately measure the vector components of the magnetic field simultaneously at several points on a planar surface. This capability allows us to estimate gradient fields along all three directions using the central point finite different approach along two x and y directions. The existing receiver placement configuration can be extended along third direction by adding two receivers along the z-axis as well. This extension provides the ability to estimate tensor gradients along all three coordinate axes, and, therefore, to estimate the transmitter's location analytically. The full magnetic field gradient is estimated using the finite difference approach (see Figure 3), as:

$$\frac{\partial \mathbf{H}_o}{\partial x} = \frac{\mathbf{H}_2 - \mathbf{H}_1}{2dx}$$

$$\frac{\partial \mathbf{H}_o}{\partial y} = \frac{\mathbf{H}_4 - \mathbf{H}_3}{2dy}$$

$$\frac{\partial \mathbf{H}_o}{\partial z} = \frac{\mathbf{H}_6 - \mathbf{H}_5}{2dz}$$

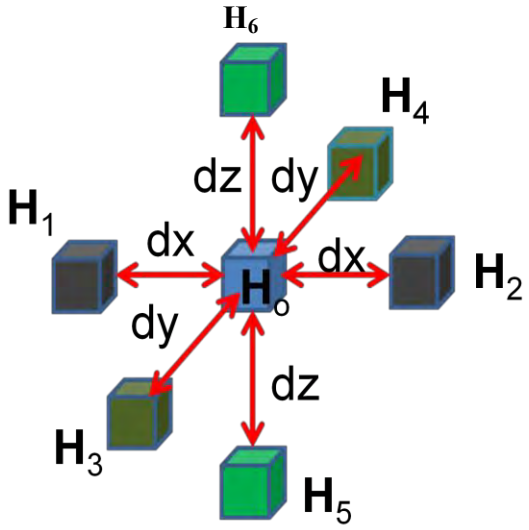

Figure 3. Schematic diagram for estimating the full magnetic field gradient tensor using the finite different approach and the seven vector receivers.

Note that the proposed receiver configuration could also be used for locating objects of interest during the transmitter off time.

2.4.2 Five vector receivers approach

In the quasi-magneto static regime we assume that the magnetic field is irrotational, thus:

$$\nabla \times \mathbf{H} = 0$$
$$\nabla \cdot \mathbf{H} = 0 \qquad (2.11)$$

From here follows:

$$\frac{\partial H_x}{\partial z} = \frac{\partial H_z}{\partial x};$$
$$\frac{\partial H_y}{\partial z} = \frac{\partial H_z}{\partial y};$$
$$\frac{\partial H_z}{\partial z} = -\left(\frac{\partial H_x}{\partial x} + \frac{\partial H_y}{\partial y} \right) \qquad (2.12)$$

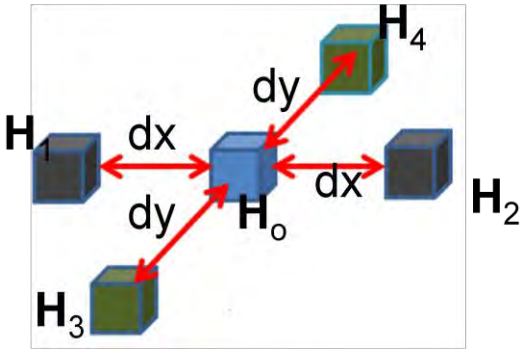

Figure 4. Schematic diagram for estimating the full magnetic field gradient tensor using the finite different approach and the five vector receivers.

From(2.12), follows that under the magneto quasi static assumption, the magnetic fields derivatives with respect to the z coordinate can be expressed using derivatives with respect to x and y coordinates at five point (see Figure 4) . Under this assumption, the number of receivers is reduced from seven to five and they are placed them in a in the same plane.

2.5 Estimating Tx location using nonlinear optimization techniques

The previously mentioned approach for determining an underwater detection system's location is based on the assumption that the Tx behaves like a magnetic dipole. However, when the receivers are close (~ less then three times of characteristic length) to the transmitter, the assumption breaks down. In order to overcome this and to measure geo-location precisely, a non-linear optimization approach is needed. The primary magnetic field produced by the Tx coil depends nonlinearly on the Tx location and orientation, and therefore determining a buried object's orientation and location is a non-linear problem. Inverse-scattering approaches are carried out by determining an objective function [25]–[27] as a goodness of fit measure between the primary $\mathbf{H}^{pr}$ and measured $\mathbf{d}^{m}$ magnetic field data:

$$\text{minimize} \quad \phi(\mathbf{v}) = \left\| \mathbf{d}^{m} - \mathbf{H}^{pr}(\mathbf{v}) \right\|^{2}. \qquad (2.13)$$

where **v** is location and orientation of the Tx coil.

2.5.1 A gradient search technique

One of the most popular approaches for solving inverse problems is the gradient method [25]–[27]. The gradient method requires the system's Jacobian, which contains gradients of the scattered field relative to the unknown parameters of interest. Since we have an analytical expression for the primary magnetic field, this allows us to calculate these gradients analytically without any complications. Let us assume that v is a set of Tx parameters (orientation and location which must be determined from a set of measured data $\{\mathbf{d}^{m}\}$. A convenient way to view the problem is to define a forward map as one that associates a given v with an initial v_o value. Here it is understood that the evaluation of predicted data in the first step is through the initial v_o value. A least-squares formulation of this problem identifies a minimum of the error function, by solution of the equation:

$$\left[\frac{\partial \mathbf{H}^{pr}}{\partial v}\right]_{v_{\beta-1}} \delta v [redacted] \mathbf{d}^{m} \quad \mathbf{H}^{pr}(\{v_{\ 1}\}) \qquad (2.14)$$

where $J_{v_{\beta-1}}$ is a Jacobian matrix based on {vβ-1}, β is the iteration number, $\{\delta \mathrm{v}_{\beta}\}$ is a vector of incremental steps in unknown parameter values, to be determined from (2.14); and the primary magnetic field values $\{\mathbf{H}^{pr}\{\mathrm{v}_{\beta-1}\}\}$ are predicted based on $\{\mathrm{v}_{\beta-1}\}$. Using iterative procedures, the $\{\mathrm{v}_{\beta}\}$ parameters are updated as:

$$v_{\beta} = v_{\beta-1} + \delta v_{\beta} \ . \qquad (2.15)$$

2.5.2 A global optimization technique

In many cases the standard gradient search approaches suffer with a local minima problem and sometimes lead to inverting incorrect location and orientation. To avoid this problem, recently a different class of global optimization search algorithms has been developed. One such technique is the DE method [28]-[29]. DE is a heuristic, parallel, direct-search method for minimizing nonlinear functions of continuous variables. It is very easy to implement and has good convergence properties. We used the DE algorithm with the primary magnetic field to determine the underwater detection systems geo-location by minimizing an objective function (2.13). The algorithm iterates minimize the objective function (the difference between measured and model data).

2.6 The Method of Auxiliary Sources for assessing EMI noise due to the marine environment

The main objective of the work described in this section is to assess the noise level due to the marine environment in underwater geo-location. Marine environments tend to exhibit several electrically different layers because of salt intrusions, haline fronts in shallow areas like river estuaries, and bottom layers. Salt intrusions and fingers as well as haline fronts are typical of the coastal ocean and result in high salinity gradients. The EMI field thus behaves in a marine environment much as it does in a layered medium. Strong vertical salinity gradients produce EM noise i.e. the false-alarm ratio, and reduce the effectiveness of the geo-location system. The investigation is undertaken in frequency regime using the MAS with a surface impedance boundary condition. The studies are carried out using square loop Tx loop. Namely, we studied how air water interface affects on the proposed geo-location system performance, and how the underwater UXO like metallic targets will change the primary magnetic field, the surface roughness effects are also considered and analyzed.

The Method of Auxiliary Sources (MAS) is a numerical technique originally designed for solving various electromagnetic radiation and scattering problems. The MAS is robust, easy to implement, and accurate, and has been used to investigate waveguide structures, antennas, scattering, electromagnetic wave propagation in complex media, etc. It has also been employed successfully in the analysis of low-frequency electromagnetic induction scattering phenomena [9],[10]. In the MAS, boundary value problems are solved numerically by representing the electromagnetic fields in each domain of the structure under investigation by a finite linear combination of analytical solutions of the relevant field equations, corresponding to sources situated at some distance away from the boundaries of each domain. The “auxiliary sources” producing these analytical solutions are chosen to be elementary dipoles/charges located on fictitious auxiliary surface(s) that usually conform to the actual surface(s) of the structure. In practice, at least as the method is realized here, we only require points on the auxiliary and actual surfaces; thus we do not need to the detailed mesh structures required by other methods. Figure 5 illustrates the MAS as applied to the UW environment.

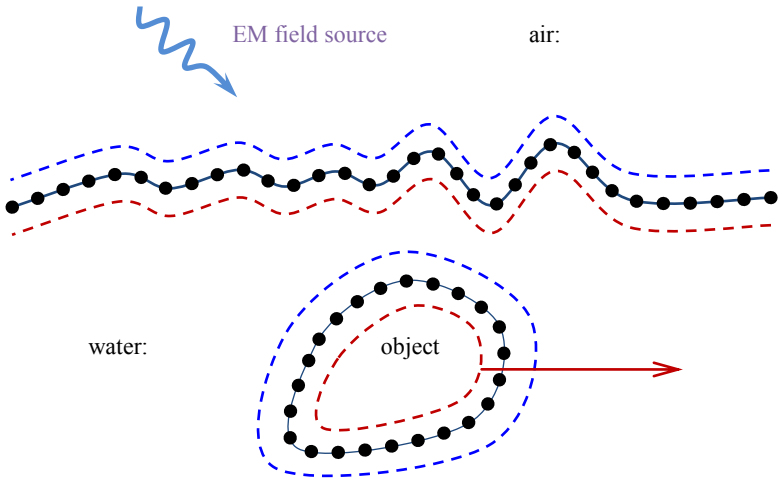

Figure 5. The MAS applied to underwater detection problem. For every boundary between the domains with different physical properties (air-water interface, object surface) a set of auxiliary surfaces is defined which are conformal to the corresponding boundary. EM fields in air are created by the external EM field source and the auxiliary sources located at the surface . The fields inside water are described as the superposition of fields created by sources located at and . Finally, the fields inside the object are represented by the auxiliary sources on .

Therefore, for every physical boundary in the problem of interest there are two layers of auxiliary sources: the inner layer of sources, which describes the EM fields outside of this boundary, and the outer layer that describes the fields in the space confined by this boundary. Therefore, at any location in space the electric and magnetic fields can be represented as a superposition of fields created by the independent EM field sources and auxiliary sources:

$$\boldsymbol{E}\ \boldsymbol{r}\ = \boldsymbol{E}_{source}\ \boldsymbol{r}\ + \sum_n A_n \boldsymbol{G}_E\ \boldsymbol{r}, \boldsymbol{r}_n \,|\, \boldsymbol{\tau}_n \tag{2.16}$$

$$\boldsymbol{H}\ \boldsymbol{r}\ = \boldsymbol{H}_{source}\ \boldsymbol{r}\ + \sum_n A_n \boldsymbol{G}_H\ \boldsymbol{r}, \boldsymbol{r}_n \,|\, \boldsymbol{\tau}_n \tag{2.17}$$

where $\boldsymbol{G}_E\ \boldsymbol{r}, \boldsymbol{r}_n \,|\, \boldsymbol{\tau}_n$ and are the electric and magnetic fields, respectively, created by a unit auxiliary source located at and oriented along the surface tangent , while are the unknown amplitudes of the auxiliary sources. The summation is performed over all auxiliary sources which are *external* to the current domain. The only constraint placed on the fields is to satisfy the boundary conditions for Maxwell's equations:

(2.18)

which can be evaluated at a finite number of collocation points across the object boundaries, leading to a system of linear equations binding together the amplitudes of the auxiliary sources . The scattering problem is solved once these amplitudes are found, since any other EM parameter of interest can be derived through the EM fields expressed using Eqs (2.16) and (2.17) . This scheme also provides an easy way of monitoring the accuracy of the solution by observing the boundary condition mismatch in the areas between the collocation points.

Usually, EMI scattering responses are expressed relative to the induction number $\chi \equiv \sqrt{-2j\pi\nu\sigma\mu}\, a$, where j is the imaginary unit, a (m) is a characteristic dimension of the object (usually the smallest), ν (Hz) is the frequency, $\mu = \mu_o\mu_r$ (H/m) is the magnetic permeability, and σ (S/m) is the scatterer's electrical conductivity. The quantity χ is proportional to a/δ, where δ(m) is the skin depth. It is very well established that the electromagnetic field in the interior domain decays over distances on the order of the skin depth (high induction number). This reduces the efficiency and accuracy of the MAS. To overcome this problem, a combined MAS/surface impedance boundary condition (MAS/SIBC)[24] has been developed and widely used for solving a variety of EMI problems at frequencies ranging from 0 Hz (magnetostatic regime) up to 1 MHz. The SIBC relates the tangential components of the electric **E** and magnetic **H** fields on the surface, as:

$$\mathbf{E}_t = [-(1+j)/\sigma\delta]\hat{\mathbf{z}} \times \mathbf{H}_t \tag{2.19}$$

where the subscript t indicates the component tangential to the surface of the conductor. With $\hat{\mathbf{n}} = -\hat{\mathbf{z}}$ the outward pointing unit vector normal to the surface, $\mathbf{E}_t = -\hat{\mathbf{n}} \times (\hat{\mathbf{n}} \times \mathbf{E})$ and (2.19) becomes:

$$\hat{\mathbf{n}} \times (\hat{\mathbf{n}} \times \mathbf{E}) = [-(1+j)/\sigma\delta]\hat{\mathbf{n}} \times \mathbf{H}\,. \tag{2.20}$$

3 RESULTS AND ACCOMPLISHMENTS

In this chapter, we present numerical results to understand the proposed underwater Geo-location system's performance in conducting environment. Namely, we investigated in great detail: how discontinuous conductivity (i.e. air/ water interface) changes the primary magnetic field in a conducting environment; how the transmitted signal changes as a function of frequency; what is the best separation between Rx sensors for estimating the magnetic field full tensor gradient; how noise due to highly conducting metallic objects affects the proposed underwater geo-location algorithm; how the proposed algorithm depends on the Tx coils size and separations; what is the system limitation in terms of conductivity, the distance and noise. We have addressed these issues using analytical and numerical models and simple experiments.

Computer algorithms utilized here are based on the finite difference technique for the magnetic field full tensor gradient estimation and the MAS for exploring the system's performance in underwater environments. Namely, we investigated how air/water surface roughness affects the transmitted EMI signal, what are optimal frequencies for underwater Geo-location, and how high conducting and permeable metallic UXO-like objects influence the system. These provided detailed information on the proposed geo-location system's performance and on the full tensor gradient based algorithm applicability. Our studies demonstrated that the vector magnetic field full tensor gradient method for estimating geo-location is very sensitive to the noise due to frequency, conductivity of the water and distance between the sensor and Tx. This forced us to deploy a non-linear optimization algorithm for estimating the position algorithm. The non-linear algorithm provides precise and accurate locations up to twenty meters at low frequencies without knowing water's conductivity. The algorithm is robust and applicable for underwater environments.

3.1 Effects of Tx size and frequency

In this section we describe how we investigated the transmitted EMI field changes as a function of Tx coils size, and frequency. We started this with understanding the interaction between the circular loop coil and the air/water interface using the analytical solutions provided by **[12].** The transmitter loop, which is considered as an infinitely thin wire is placed at 5 cm above the air/water interface. For this demonstration, the water has parameters: conductivity $\sigma = 4$ [Siemens/meter, S/m], permeability $\mu_r = 1$. The sensors operating frequencies are 40 Hz and 100 Hz. The transmitted field versus distance from the air/water interface to 50 meters inside salt water is depicted on Figure 6. The results show that as the radius of the transmitter loops increases, the magnetic field's value increases as well. In addition, these studies demonstrate that as frequency increases the transmitted magnetic fields value decreases as distance between the sensor and observation points increases (see Figure 6 right).

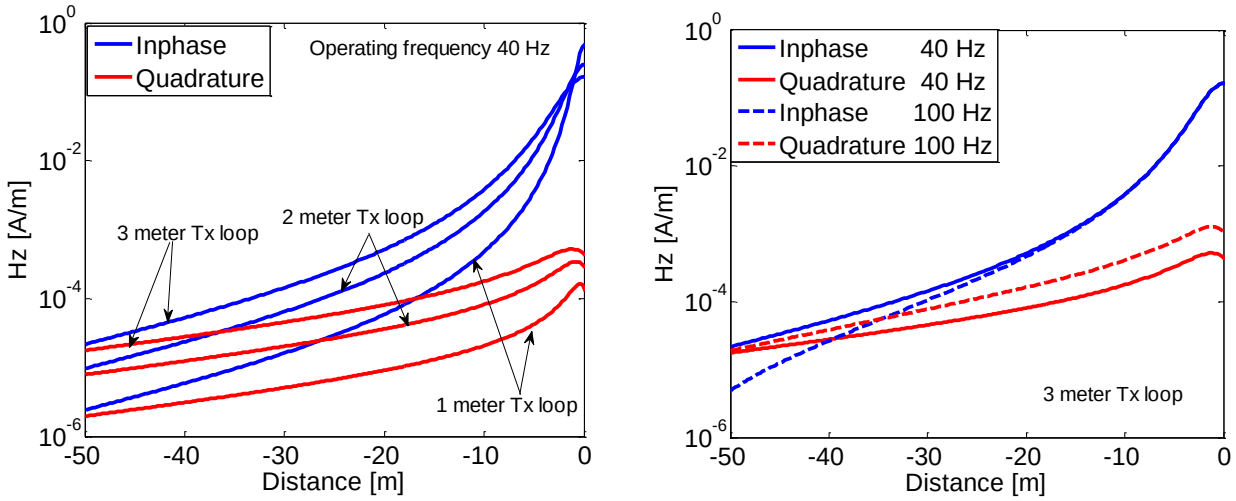

Figure 6. The Transmitted magnetic field versus distance inside salt water at 40 Hz for different loop sizes (left), and for 3 meter loop at 40 Hz and 100 Hz frequencies (right).

We conducted systematic studies for square shaped Tx coils at various sizes and at different frequencies. The Tx coil was placed inside a conducting environment. The objective of these investigations was to understand how the primary magnetic fields depend on the sensor size, the frequency, and distance between Rx and Tx. The results are depicted on Figure 7 and Figure 8.

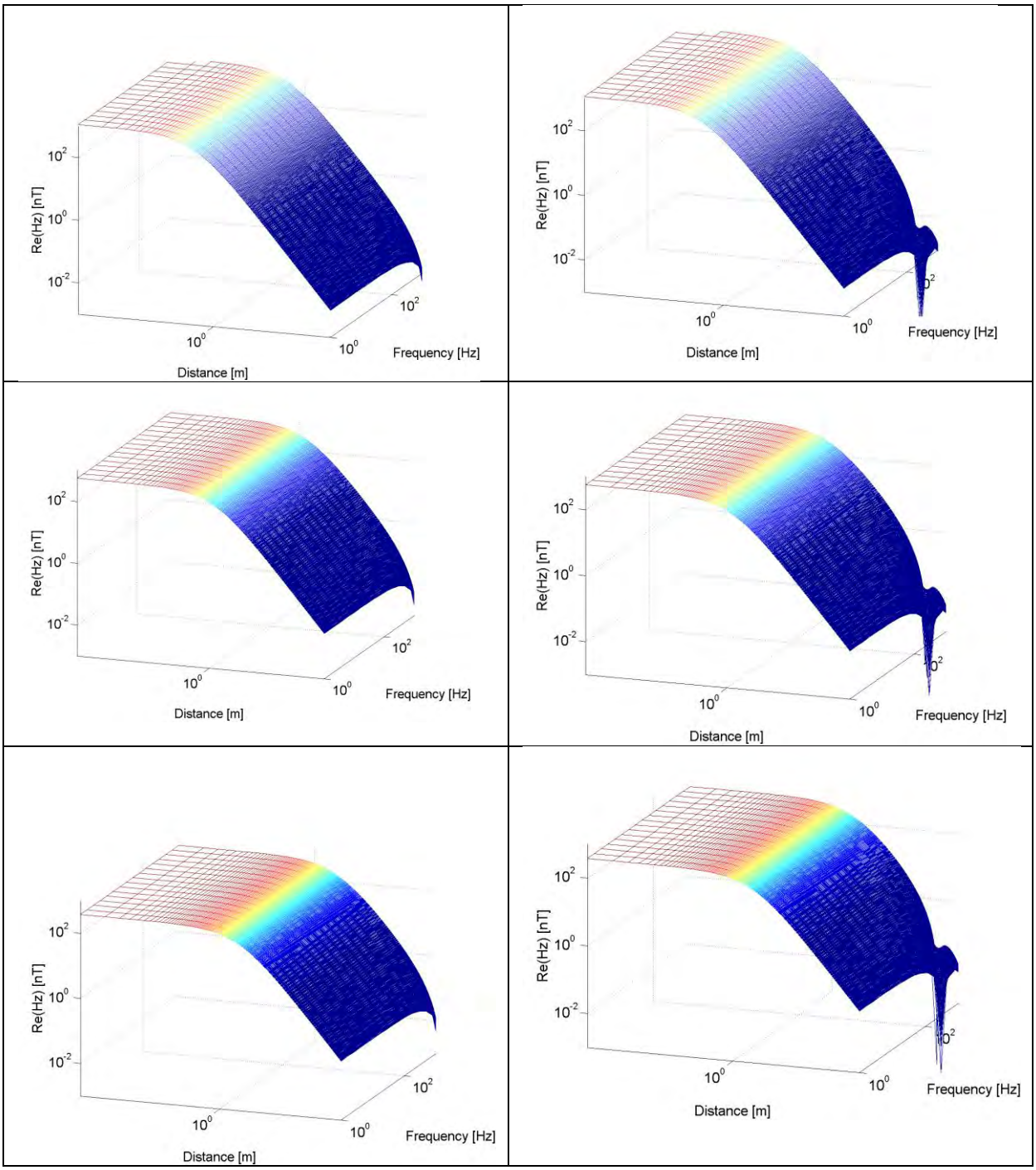

Figure 7. The Transmitted magnetic field for three (1mx1m first raw, 2m x 2m second and 3m x 3m third raw) different sized Tx coils versus distance and frequency inside 1 S/m (left column) and 4 S/m (right column) salt water.

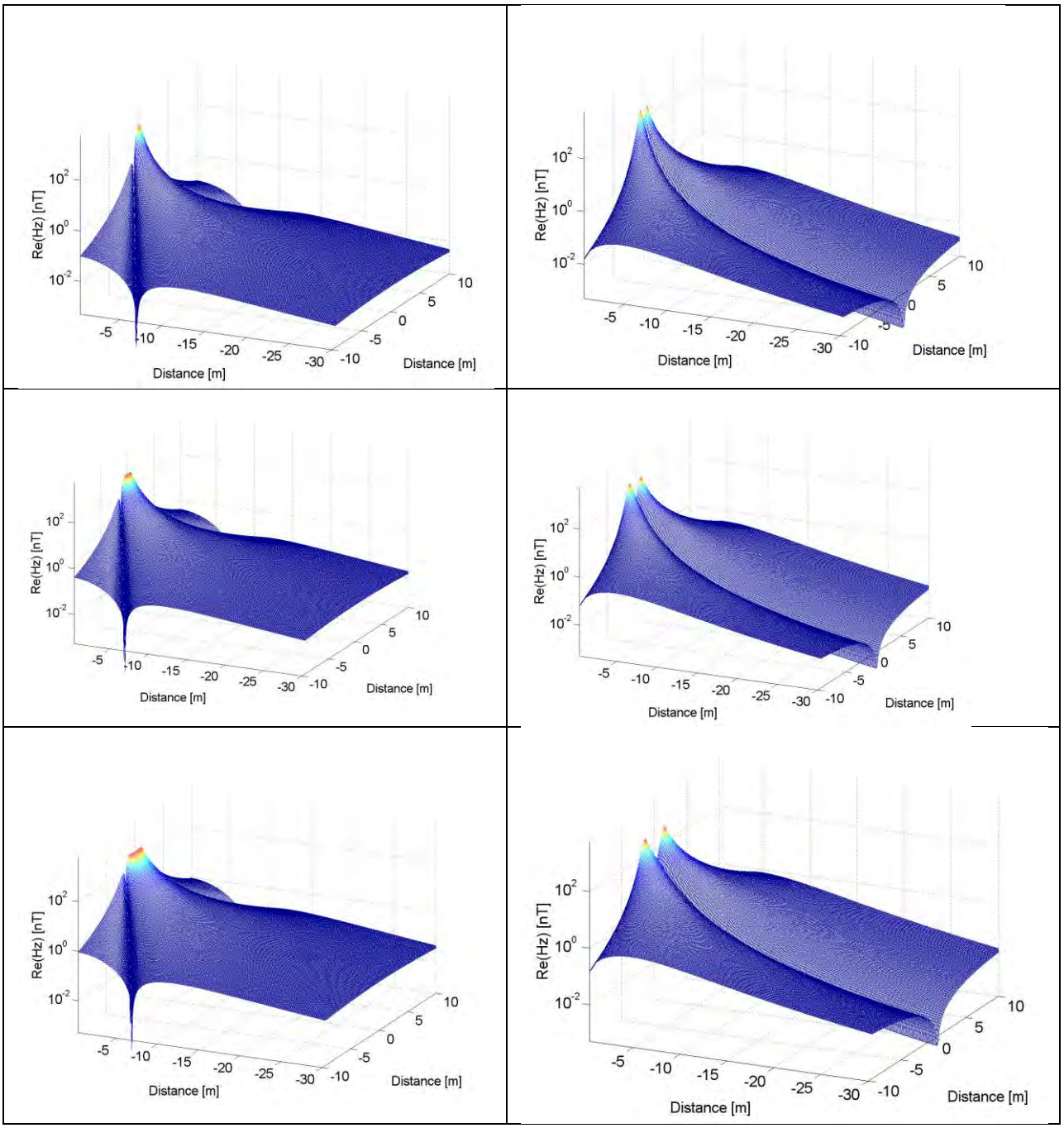

Figure 8. The Transmitted magnetic field real parts at 100 Hz for three (1mx1m first row, 2m x 2m second and 3m x 3m third row) different size Tx coils versus distances 1 S/m salt water.

These results show that the transmitted primary magnetic fields strongly depend on the frequency and Tx size. As frequency and distance increase, the transmitted magnetic field values start changing (Figure 7), which indicates that at high frequencies and long distances for geo-location, the conducting mediums' conductivities are needed. The results also illustrate that (Figure 8) the transmitted primary magnetic fields' magnitudes are small near the Tx but as distance from the Tx increases, the primary field from a big transmitter is increasing. This can be explained by two reasons : first, at far distances the Tx behaves like a dipole; and second, as the size of Tx increases the magnetic moment increases which in return produces a large magnetic field.

3.2 Surface roughness effects

In this section we illustrate how surface roughness affects EMI signals. All calculations are done using the 3D MAS code. For this reason we conducted two sets of simulations with the source of electromagnetic fields being (i) a square loop in the *xy* plane, located above the water surface and (ii) a single *x*-oriented magnetic dipole located underwater. The level z=0.0 m was assumed to be the elevation of the unperturbed water surface.

Water surface was simulated as an interference pattern from a number of surface waves with variable amplitude, wavelength, propagation direction and phase. A flat hexagonal grid was first created to provide a uniform distribution of collocation points in *xy*-plane, which is beneficial for numerical simulations (Figure 9). Then, a finite set of surface waves was applied to elevate or lower the water surface, and the resulting height-map was normalized to fit the pre-defined *wave height* (final surfaces are in Figure 10 *Wave height*):

$$z\ x,y\ =\sum_{i=1}^{N} C_i \cos\left[\blacksquare\right] + \varphi_i$$

$$z\ x,y\ = z\ x,y\ \frac{h}{\max\ \left| z\ x,y\ \right|}$$

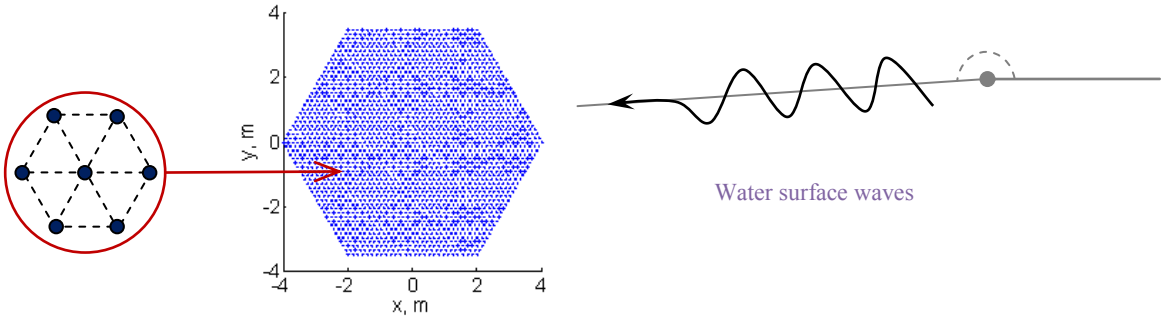

Figure 9. Flat water surface with uniform distribution of collocation points and a sample surface perturbation**.**

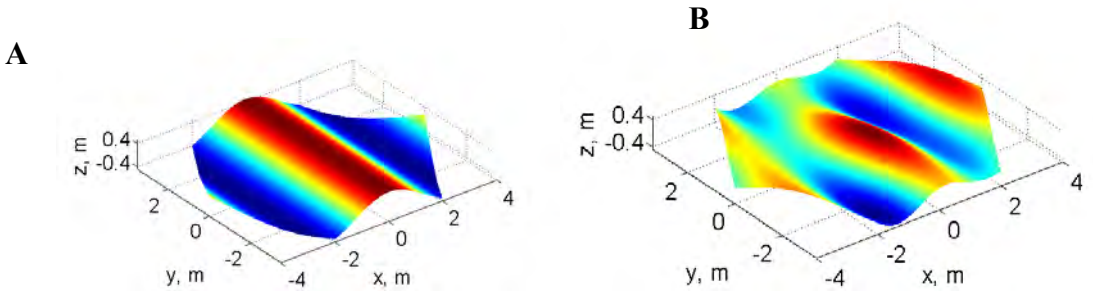

Figure 10. Simulated water surface in case of (A) single cosine perturbation; (B) interference between three surface waves in *xy*-plane having the relative amplitudes , , , wavelengths of , , , and propagating at angles of , and with respect to the x-axis.

Since in the low frequency regime the EM field wavelength is much greater than the characteristic length of the structure of interest (for , while the water surface wave wavelength ~1 m, height ~1 m, source UXO depth ~1 m, sensor array horizontal extent ~1 x 1 m), the only guiding principle for the number of collocation points is that they should describe the water surface roughness in sufficient detail. Even though the initially uniform collocation point distribution on the water surface is slightly perturbed by the oncoming surface waves, the resulting quasi-uniform distribution is still sufficient for effective use of the MAS. The total number of collocation points in our simulations was on the order of 2400, with the water surface being a hexagonal grid having the total side length of 4 m. It was found that even for such a small lateral extent the contributions from the edges of the surface may be neglected, due to the rapid decay of the magnetic fields with distance from the source. Figure 11 shows sample water surface realizations in cases of interference of three surface waves. The corresponding auxiliary surfaces are obtained from the final water surface by shifting along the normals at corresponding collocation points. The auxiliary sources are then placed along the surface tangents u, v both under and above the water.

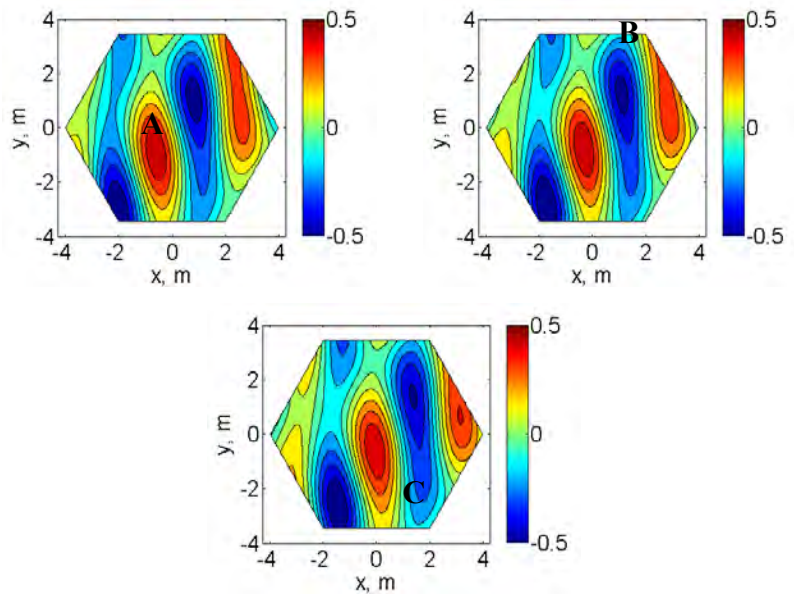

Figure 11. Water surface height realizations at different times, as a result of interference from the three surface waves as on **Figure 10 b**. Color map indicates height in meters.

Figure 12**a** shows typical MAS boundary conditions matching in our simulations. The figure shows mismatch both at collocation points and between them (total over 9000 surface points). The mismatch at collocation points is 15 orders of magnitude smaller than the value of the fields at those points, which implies high accuracy of the solution of the linear system of equations. The mismatch between the collocation points, however, is what reflects the accuracy of the solution of the physical problem, and as can be seen in Figure 12**a,** is less that 1% of the actual values of tangential magnetic fields on the water surface. Since it is computationally impossible to cover the entire water surface with collocation points, the surface coverage should stop after a certain radius. Figure 12**b** shows the typical tangential magnetic field distribution along one such "diameter" – the field on the edges is two orders of magnitude smaller than the fields of interest, and, therefore, the impact from the regions beyond the edges can be neglected.

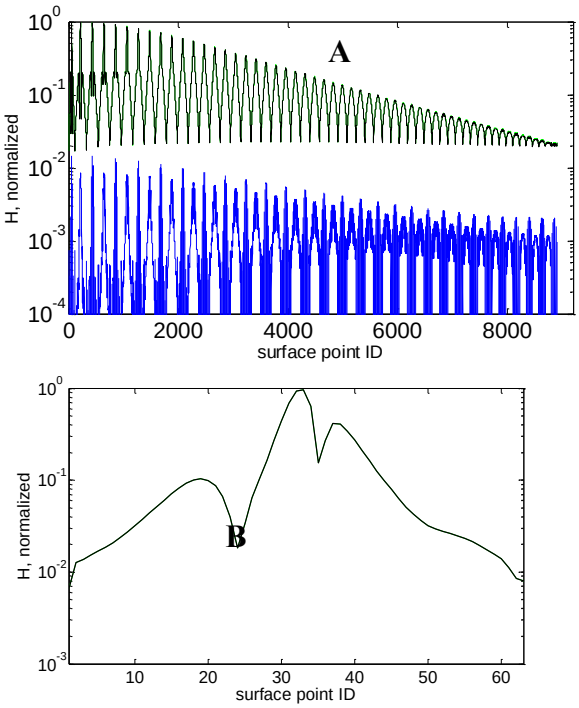

Figure 12. green (not seen) and black curves show normalized tangential components of magnetic fields below and above the water surface respectively, while blue curves show the mismatch. The mismatch is several orders of magnitude lower that the values of the fields. (B) Magnetic field distribution along the largest diameter (x=-4, …+4) of the water surface patch, for the geometry on Figure 4B. The fields on the edges of the patch are small and can be neglected**.**

Although the water surface waves perturb the magnetic field distributions at low altitudes and depths, the impact of these perturbations decays with distance. Figure 13**a** shows the total magnetic field distributions in the *xy* plane at the depth of 2 m under an unperturbed surface. The source of the magnetic field is a square current loop located 1 m above the water, frequency . Figure 13**b** shows the total magnetic field distribution at the same location in the case where the water surface is perturbed by a multiple waves with wave lengths of 3, 4 and 5 m. The bottom-to-peak height of the surface is 1 m ( ). Even though the amplitude of the water surface wave is quite high and comparable to the distances between the field source and sensors, the field distribution does not change significantly. Figure 14**a** shows the difference between magnetic fields across the sensor for flat (unperturbed) and rough (perturbed) water surfaces. The exact spatial distribution of magnetic field perturbation is asymmetric, since the source of the perturbations – the water surface – is asymmetric as well, the magnitude of the perturbation, however, is small compared to the field value itself. The magnitude of the perturbations introduced by the rough water surface is decaying with depth (Figure 14**b**).

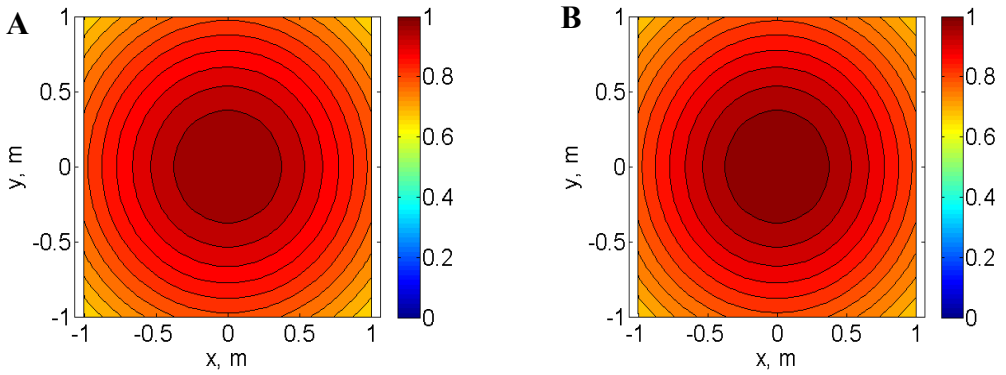

Figure 13. H-field distribution at depth 2 m below the (A) unperturbed water surface; (B) surface perturbed by multiple waves as described on Figure 4B. Fields normalized to their maximal value in the unperturbed case.

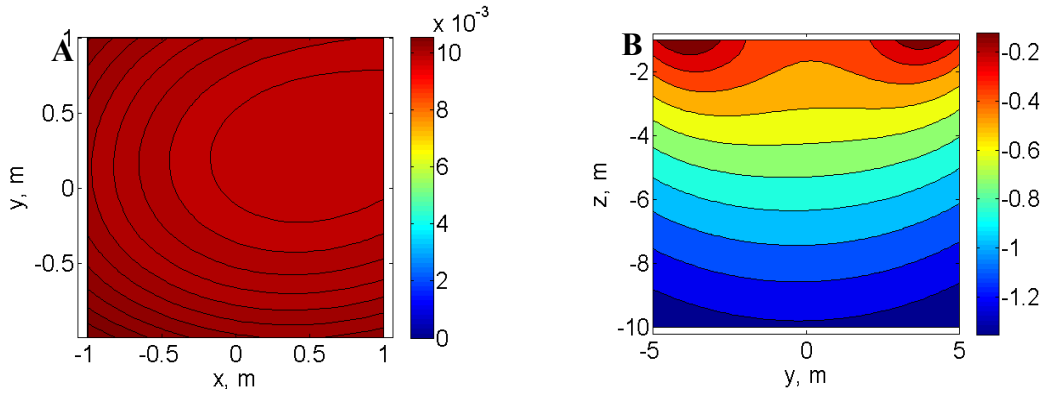

Figure 14. *(A)* Difference between magnetic H field distributions in xy-plane 2 meters below the surface in cases of unperturbed and perturbed water surfaces (normalized to the maximal field value in unperturbed case). (B) Difference between magnetic H field distributions in xz-plane in cases of unperturbed and perturbed water surfaces (normalized by the maximal value of the difference close to the water surface, log10 scale). Perturbation corresponds to multiple propagating surface water waves as on **Figure 11**.

Figure 15 shows the distribution of magnetic fields on a logarithmic scale for different surface perturbation wavelengths. This time the source of EM fields, a single *x*-oriented magnetic dipole, , was located underwater, at the depth of 1 m measuring from the level of unperturbed water surface. Figure 15A shows the distribution of total magnetic field in the entire space, assuming the water surface to be flat. The field is similar to that of a dipole in free space. In fact, however, a certain portion of field is scattered from water-air interface, and the character of this scattering depends on the shape of the interface. Figure 15B, C and D shows the scattered field below the water surface as function of its shape. Longer surface waves cause larger perturbations of scattered fields underwater. The magnitude of these perturbations, and the

scattered fields themselves, are at least 100 times smaller than corresponding transmitted fields above the water surface.

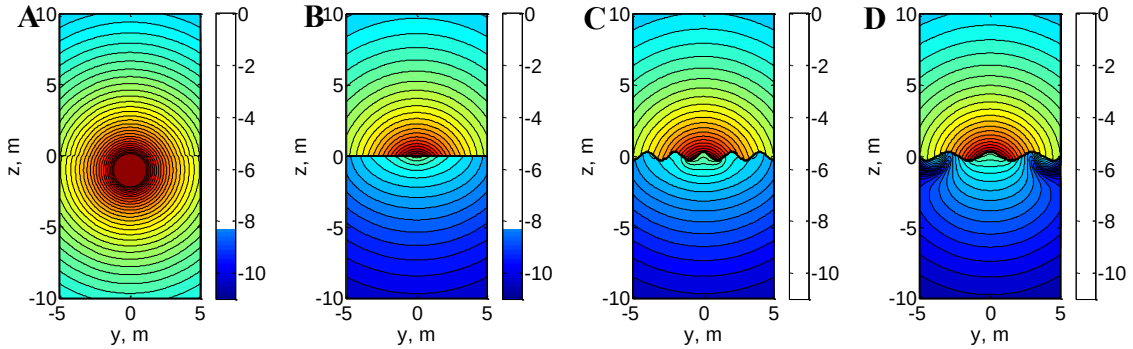

Figure 15. Normalized magnetic H field (log10 scale) distribution of an underwater dipole (x-orientation, depth 1 m). (A) total field, flat water surface; (B) total field above water, scattered field underwater, flat surface; (C) total field above water, scattered field underwater, single 2-m wavelength surface perturbation; (D) total field above water, scattered field underwater, single 3-m wavelength surface perturbation. Longer wavelength has more significant perturbation, although the magnitude of this perturbation is 4 orders of magnitude smaller than the actual value of the total magnetic field at that point.

Figure 16**A** shows the distributions of magnetic fields for a variety of frequencies in horizontal *xy* planes at various elevations above and below water surface. The source of magnetic fields is a z-oriented magnetic dipole, located 1 m above the water level in air. The upper row shows the distribution of scattered magnetic fields at this elevation in a horizontal region 2 x 2 m. The remaining three rows show the total magnetic fields diffused through the water surface at the depths of -1, -2 and -5 m. Figure 16**B**shows magnetic field distributions at same spatial locations in case of rough water surface, ranging from -30 cm to +30 cm in height. Comparison between the plots in Figure 16**A** and **B** reveals that the field distributions are not significantly perturbed by the rough water surface for low-frequency magnetic fields in the range of 1 Hz up to 10 kHz. For the frequencies higher than 100 kHz, however, the underwater field distribution is slightly changed due to the water surface roughness. At the same time, however, the conducting environment causes higher attenuation of high-frequency fields, which explains their small amplitude compared to that of the low-frequency fields. These results indicate that the perturbations in diffused and scattered EMI fields introduced by the water surface roughness are negligible and, moreover, decay with distance from the air-water interface. This interface, therefore, may be assumed to be flat in subsequent studies of UXO detection and discrimination.

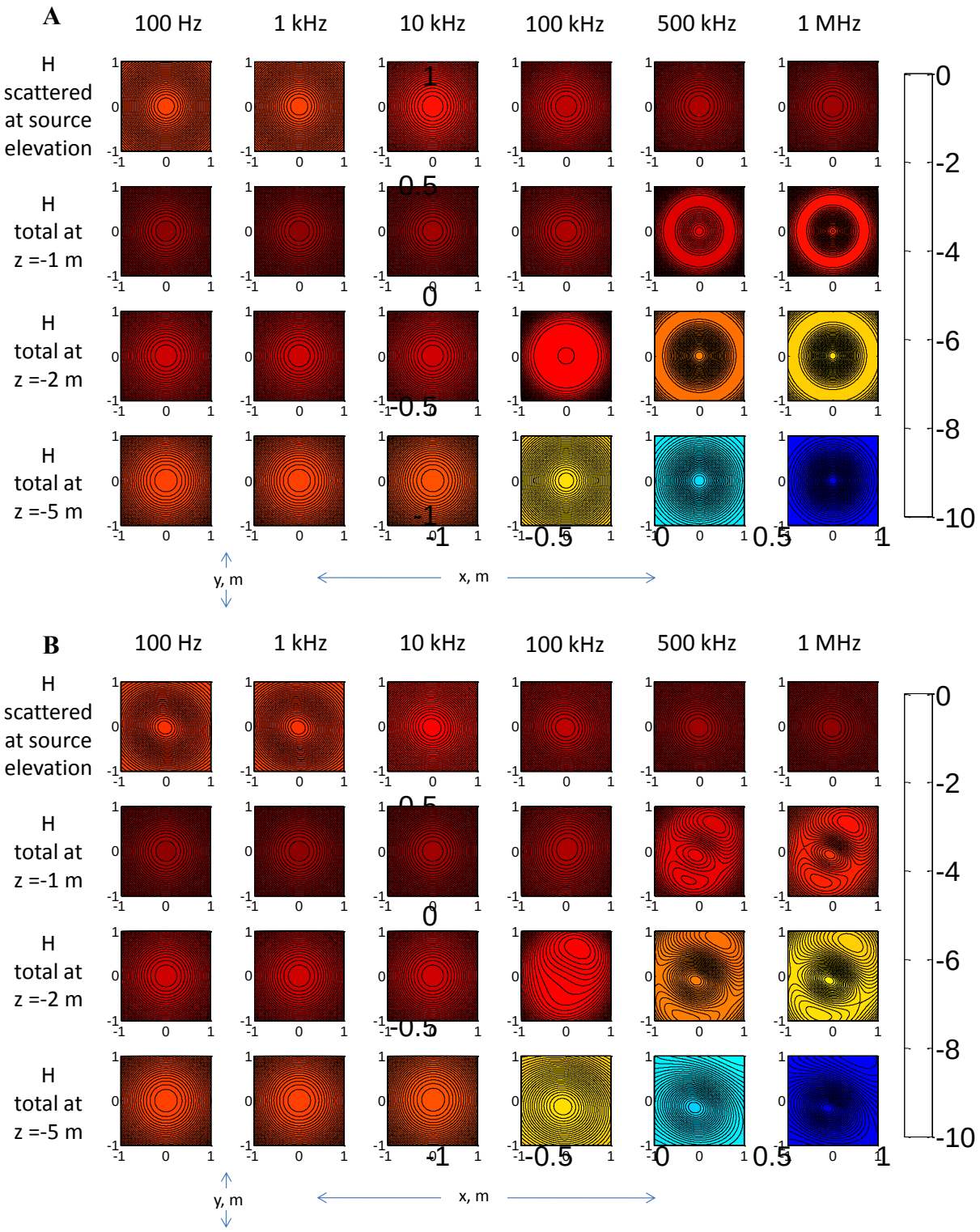

Figure 16. Magnetic H field distributions (log10 scale, normalized) in xy planes at various elevations in case of (A) unperturbed water surface and (B) perturbed surface. Field distributions are similar for frequencies below 100 kHz.

3.3 Estimating Magnetic Field's Full Tensor Gradient Using the Finite Different Approach: Error Analyses

In this section we describe how we investigated the accuracy of the finite difference approach for estimating the vector magnetic field's full tensor gradient. First, we derived the analytical expression for the primary magnetic field, due to a finite size rectangular loop, derivatives respect to x, y, and z coordinates and used it as a reference for comparisons.

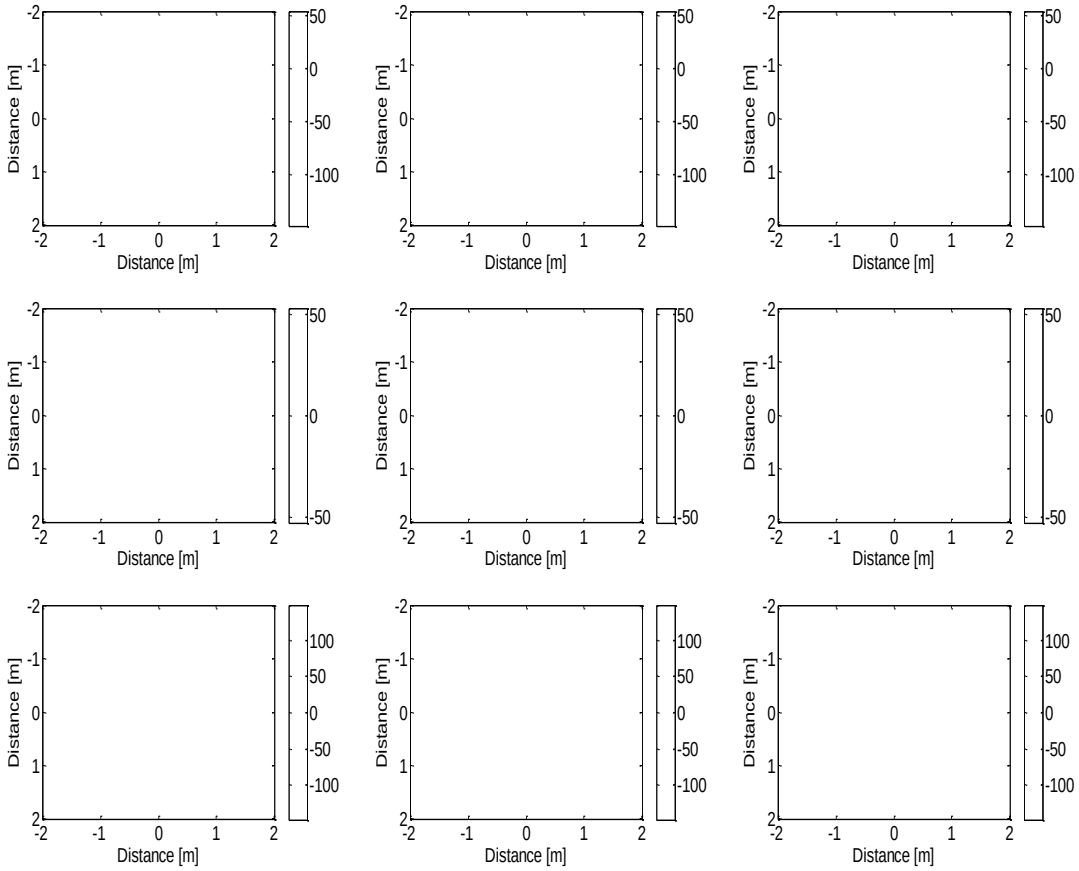

Figure 17. Derivatives respect to x, y, z coordinate for Hx, on a plane 1 meter bellow 1mx1m Tx. Left column analytical, central column numerical calculated using the finite difference approach with 1 cm separation, right column difference between the analytical and numerical.

The results are depicted on Figure 17-Figure 25. Figure 17-Figure 19 illustrate derivatives with respect to x, y and z coordinates for Hx, Hy, and Hz magnetic fields respectively, at 1 m below 1m x1m Tx coil carrying 1 A current. These derivatives are calculated analytically and

using a finite different approach with 1 cm spacing between the sensors. The comparisons between the analytical and finite difference calculations coincide as expected. Next three figures (Figure 20-Figure 22) show the comparisons at the same 1 m below plane, but with 20 cm separation between the receivers. In these cases the comparisons between the analytical and finite deference approaches shows that there are errors (see right columns). Next, we put the observation plane at 10 meters below the Tx coils and used the same 20 cm separation between the Rx for the finite deference approach. The results are shown on Figure 23, Figure 24, and Figure 25.

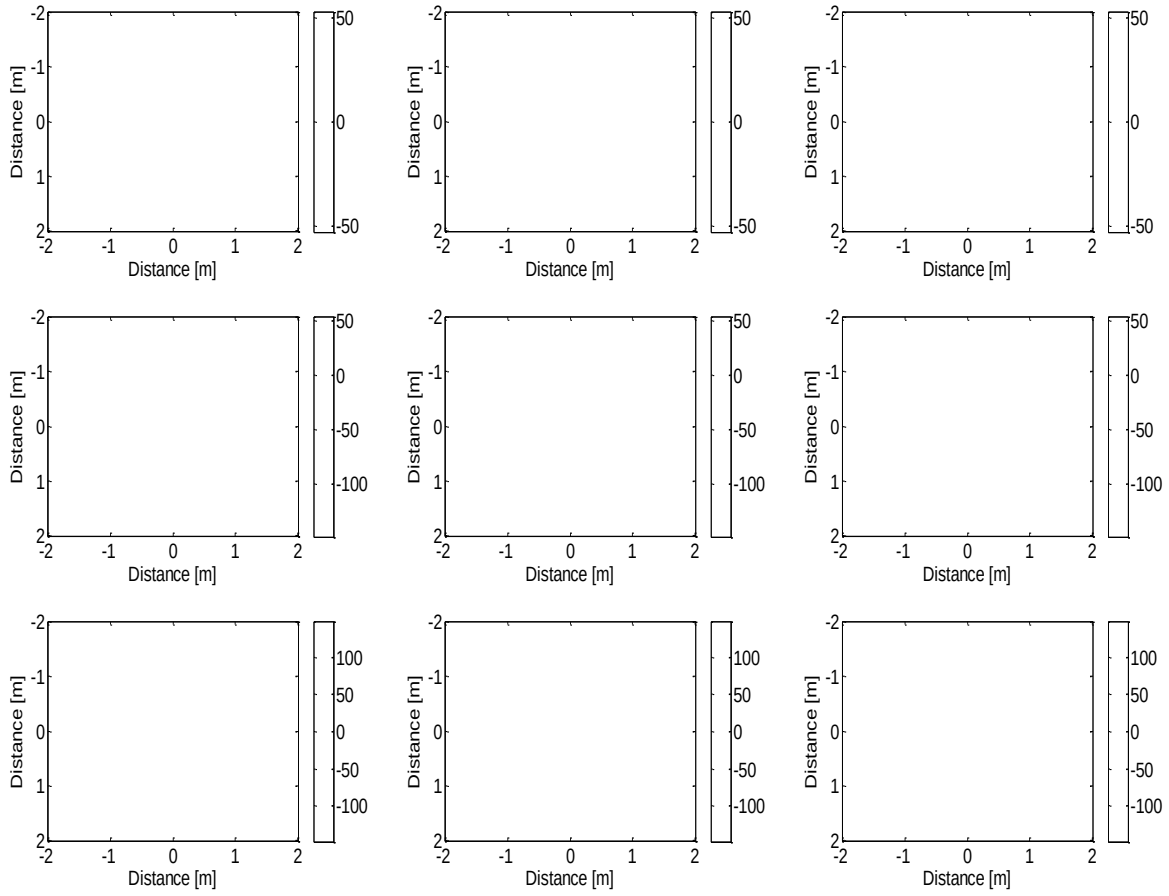

Figure 18. Derivatives respect to x, y, z coordinate for Hy on a plane 1 meter below 1mx1m Tx. Left column analytical, central column numerically calculated using the finite difference approach with 1 cm separation, right column difference between the analytical and numerical.

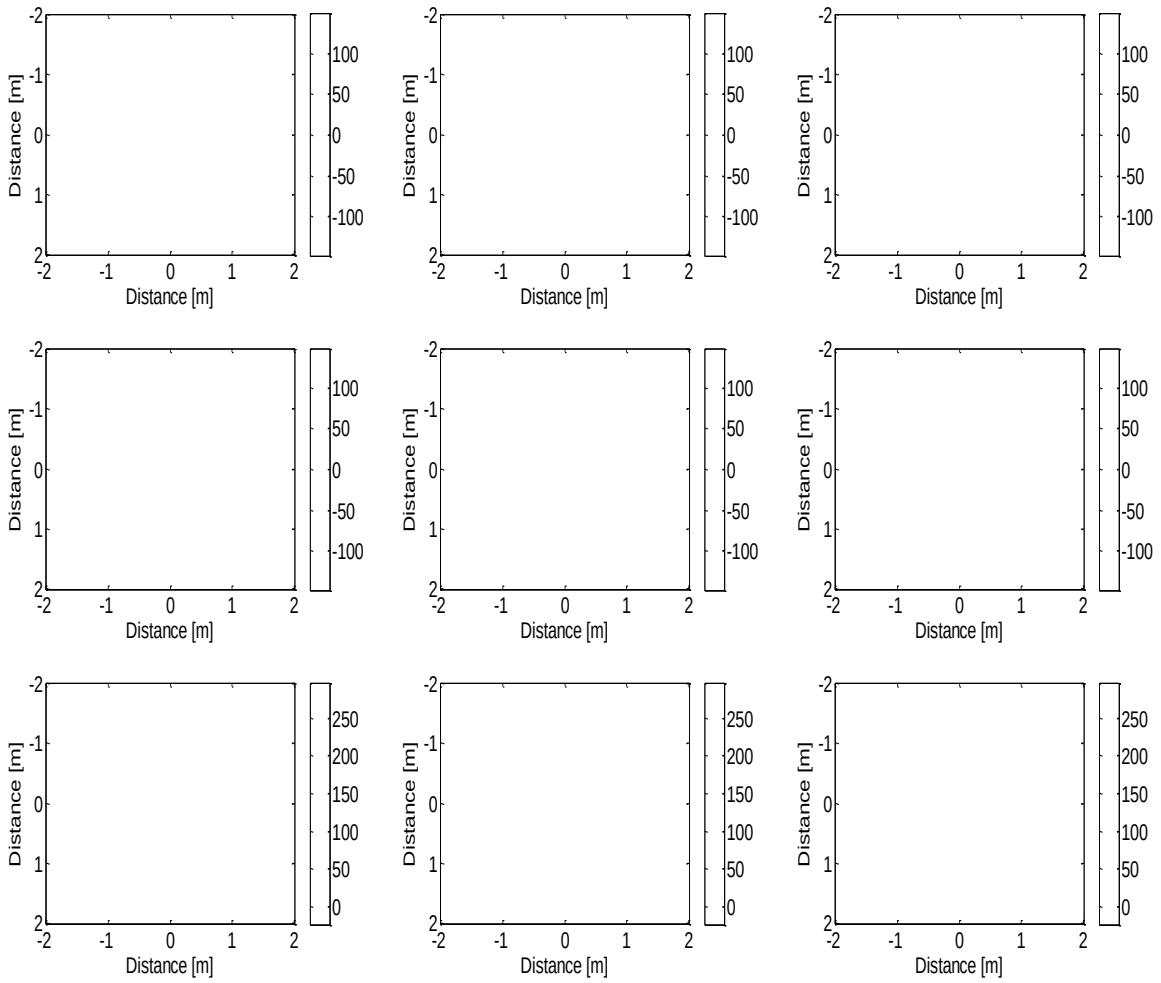

Figure 19. Derivatives respect to x, y, z coordinate for Hz on a plane 1 meter below 1mx1m Tx. Left column analytical, central column numerically calculated using the finite difference approach with 1 cm separation, right column difference between the analytical and numerical.

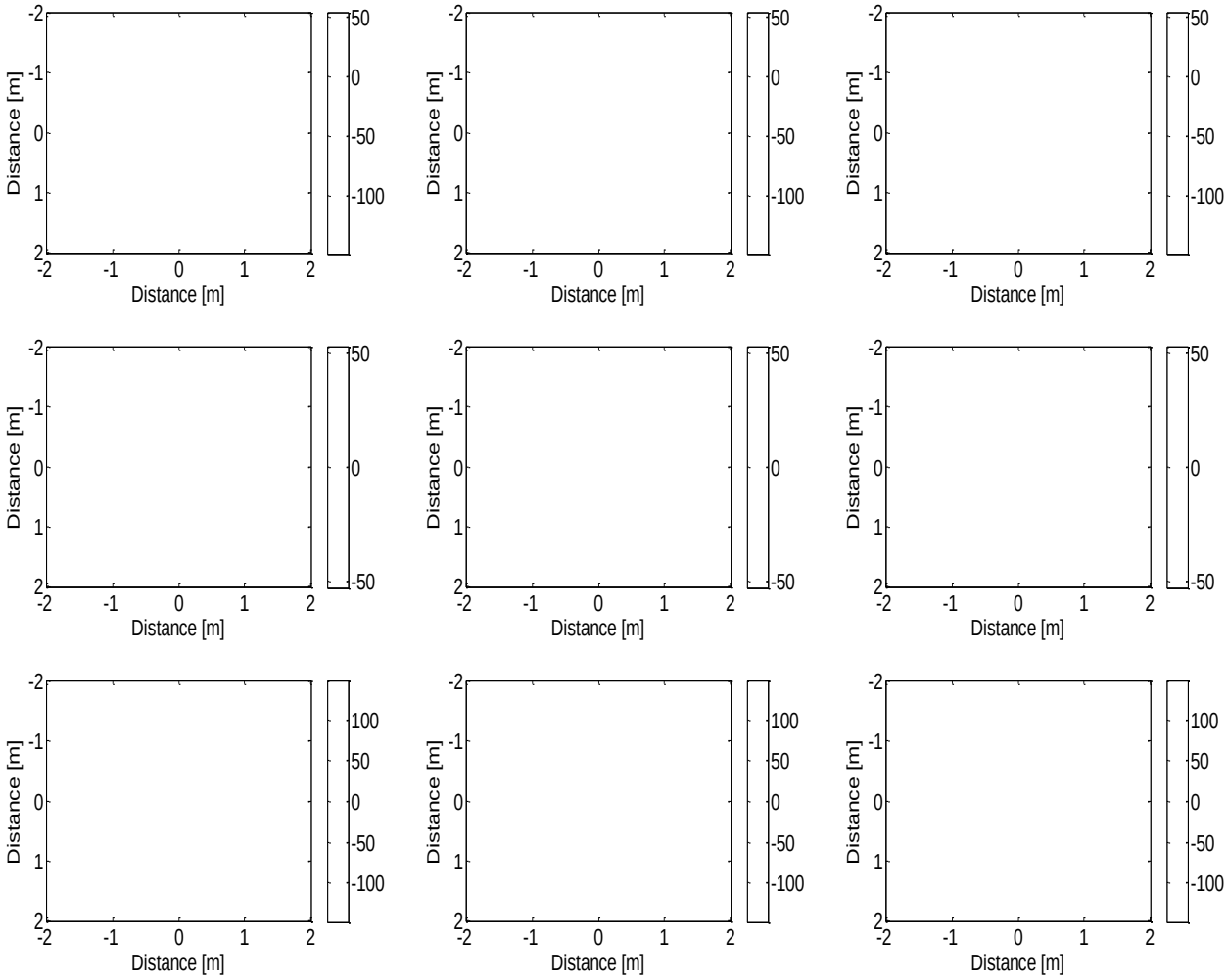

Figure 20. Derivatives respect to x, y, z coordinate for Hx, on a plane 1 meter below 1mx1m Tx. Left column analytical, central column numerically calculated using the finite difference approach with 20 cm separation, right column difference between the analytical and numerical.

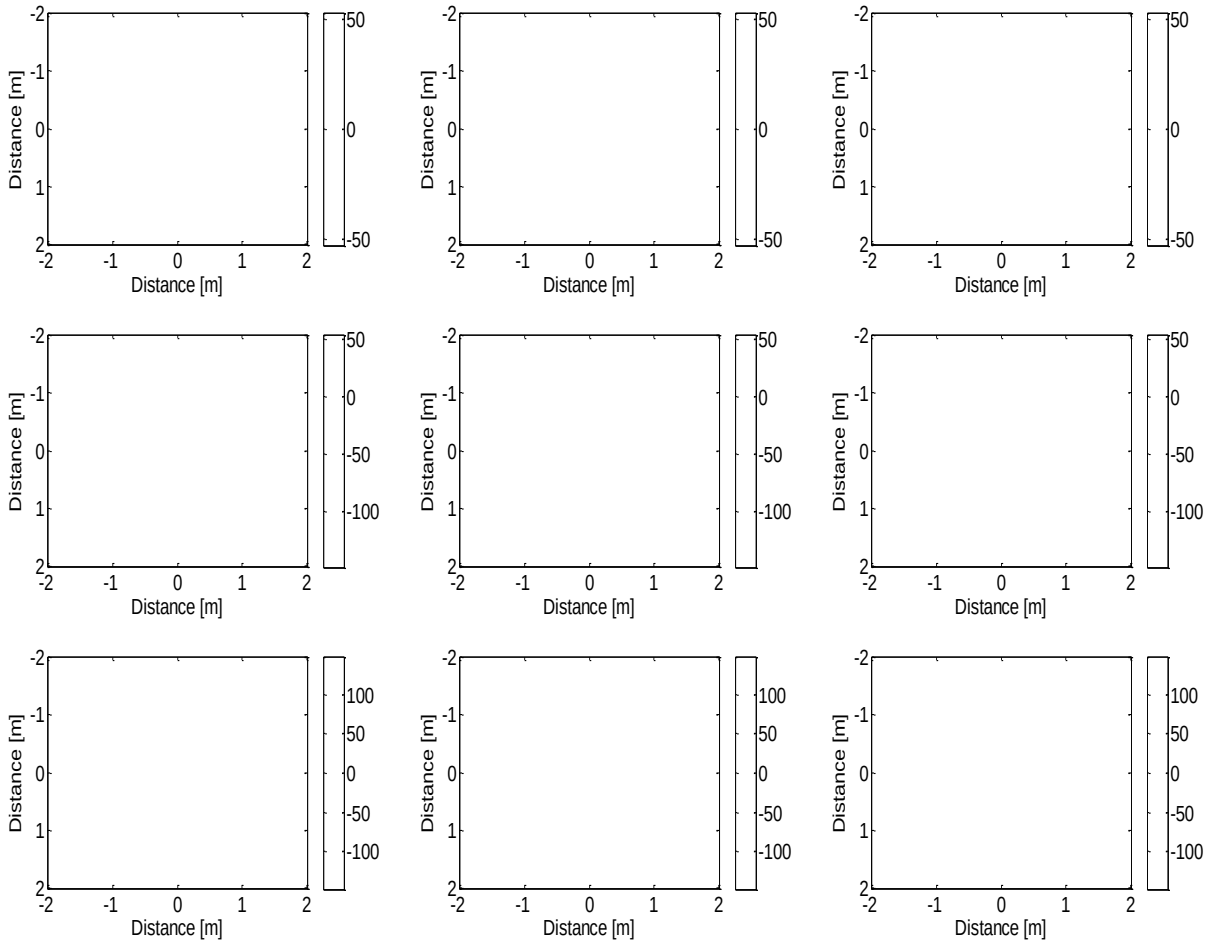

Figure 21. Derivatives with respect to x, y, z coordinate for Hy, on a plane 1 meter below 1mx1m Tx. Left column analytical, central column numerically calculated using the finite difference approach with 20 cm separation, right column difference between the analytical and numerical.

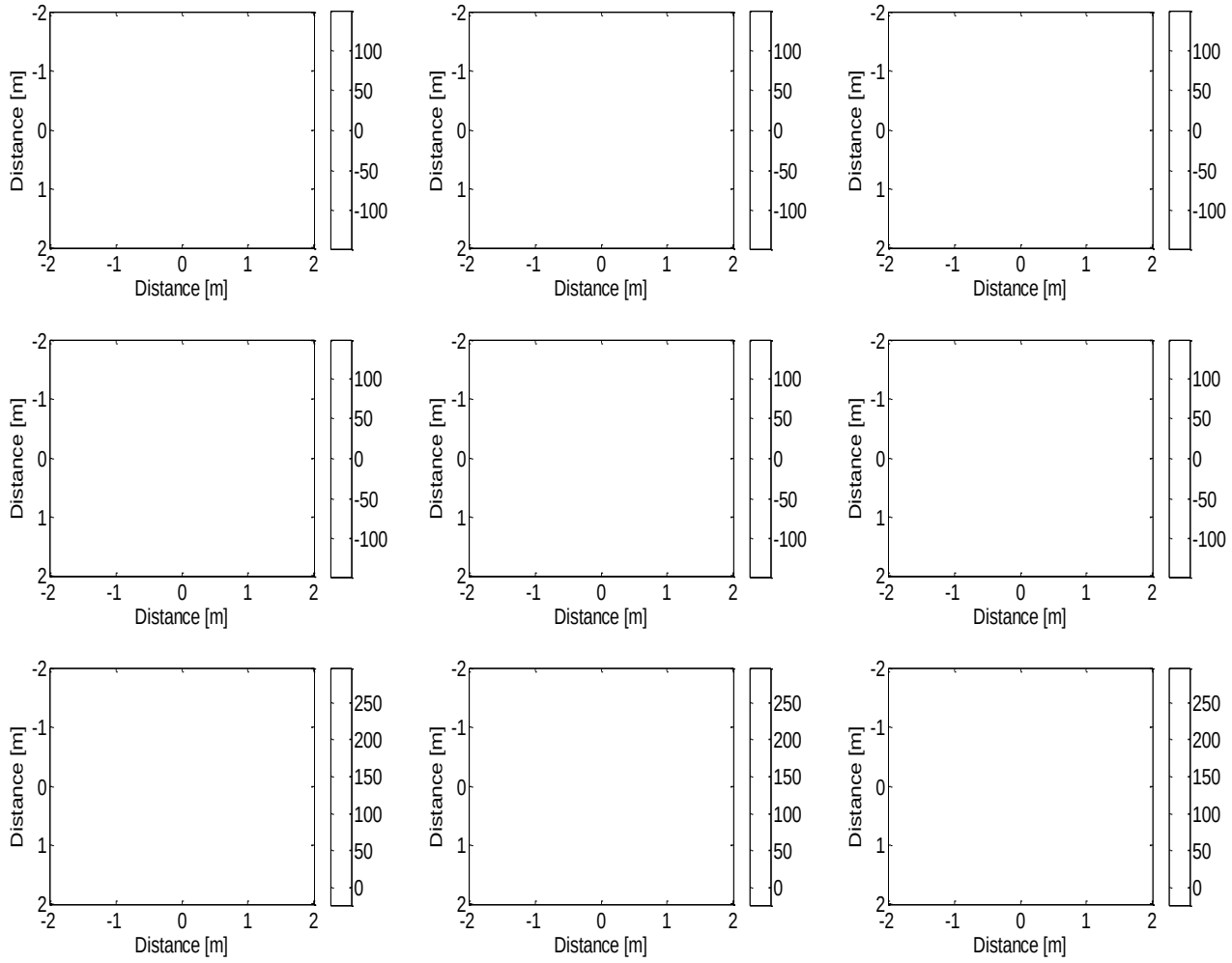

Figure 22. Derivatives respect to x, y, z coordinate for Hz on a plane 10 meter below 1mx1m Tx. Left column analytical, central column numerically calculated using the finite difference approach with 20 cm separation, right column difference between the analytical and numerical.

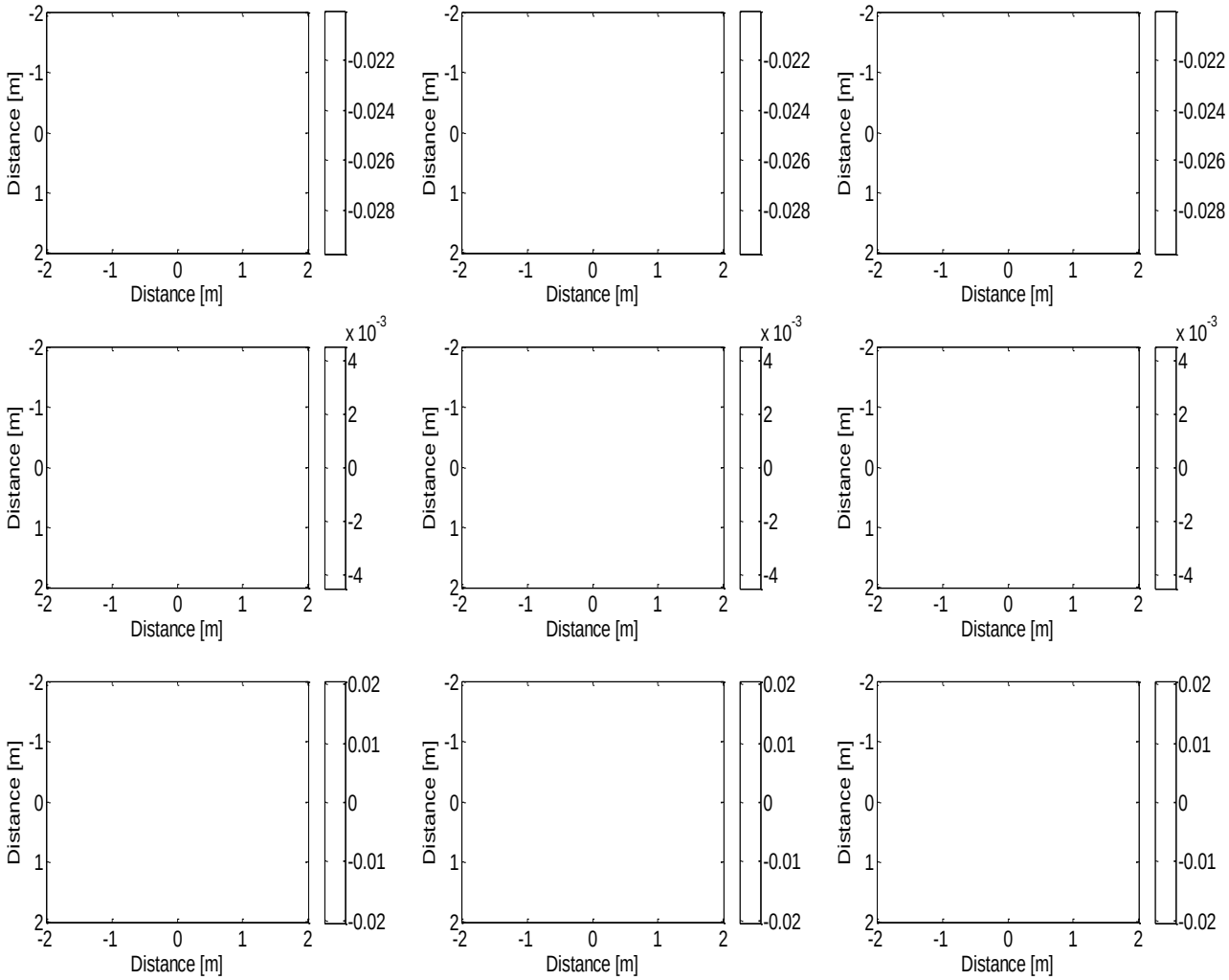

Figure 23. Derivatives respect to x, y, z coordinate for Hx, on a plane, located 10 meter below 1mx1m Tx. Left column analytical, central column numerically calculated using the finite difference approach with 20 cm separation, right column difference between the analytical and numerical.

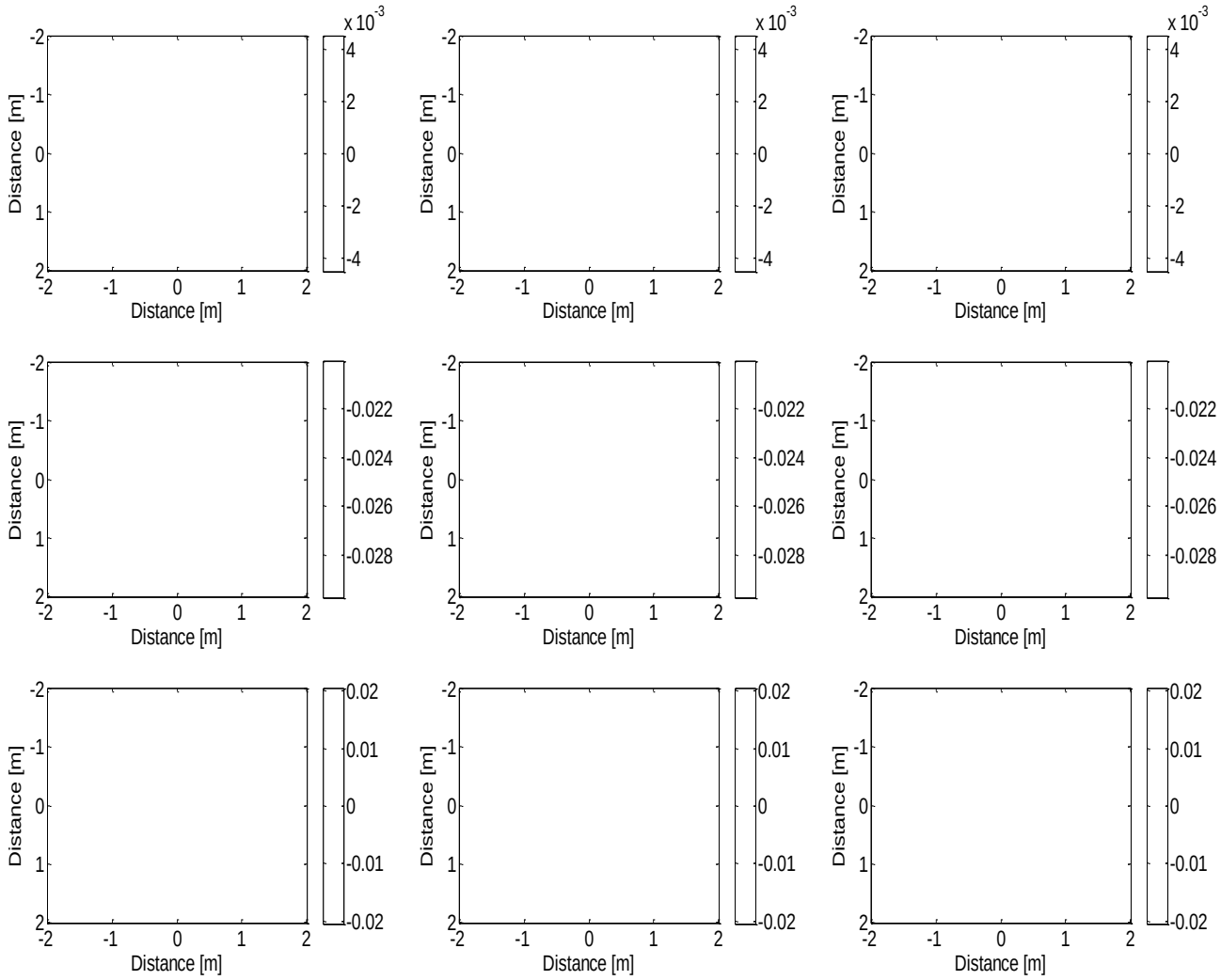

Figure 24. Derivatives respect to x, y, z coordinate for Hy, on a plane, located 10 meter below 1mx1m Tx. Left column analytical, central column numerically calculated using the finite difference approach with 20 cm separation, right column difference between the analytical and numerical**.**

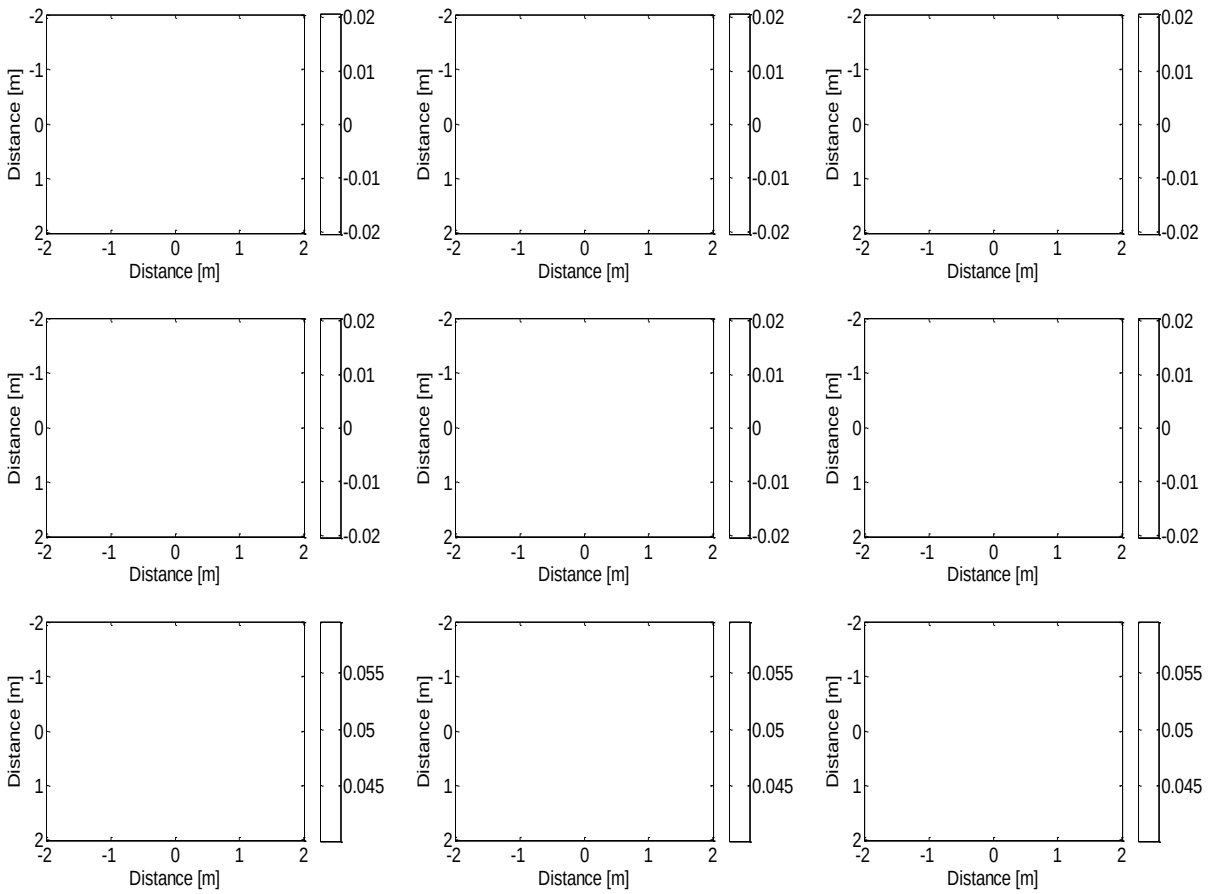

Figure 25. Derivatives respect to x, y, z coordinate for Hz, on a plane, located 10 meter below 1mx1m Tx. Left column analytical, central column numerically calculated using the finite difference approach with 20 cm separation, right column difference between the analytical and numerical.

These studies show that the finite different approach generates significant errors when the Rx are close to Tx (1 m in these studies) and separation between Rx's is more than 10cm. However when the Rx are far from the Tx (10 m here) then the finite difference approach provides even good derivatives estimation even for Rx 20 cm separation. Thus the accuracy of the full tensor gradient approach for Geo-location depends on the distance between the Rx as well as between Tx and Rx.

3.4 Assessing noise due to highly conducting and permeable underwater EMI targets

In this section we present the results for studies of how highly conducting and permeable metallic targets influence estimated underwater Rx sensor's geo-location. The problems geometry is depicted on Figure 26.

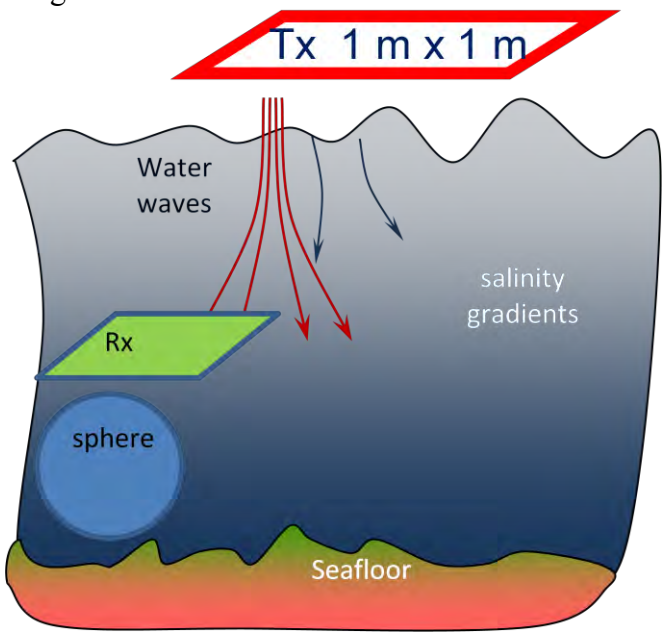

Figure 26. Schematic diagram of an EMI problem for understanding how underwater metallic targets will affect performance of the underwater geo-location system.

In these studies all distances are in meters. The real part of magnetic fields are used in (2.10) equations.

Derivatives are taken using +/- 1 point away (1 point = 2 cm), unless specified otherwise.

Figure 27. through Figure 29 show the results of the transmitter position estimation by receivers with various elevations (0.5 m, 1 m and 2 m respectively), in the case of a D=10 cm sphere scatterer at the coordinate origin. The transmitter was positioned at z=5 m (x=1 m and y=0 m are always fixed). While the position estimates can vary significantly across the receiver grid points, the largest offsets given by the sensors directly above the sphere, the mean values of the position estimates are consistent with the real transmitter position. The perturbations introduced by the sphere decay for higher receiver elevations, as expected.

Table 1 presents the receiver elevations and measured x,y, and z coordinates use for this test.

Table 1. Receiver elevations and real vs. measured location coordinates

Receiver z, m	X, m (real = 1.00)	Y, m (real = 0.00)	Z, m (real = 5.00)
50 cm	0.98 ±0.07	0.00 ±0.07	5.06 ±0.05
1 m	0.98 ±0.01	0.00 ±0.01	5.08 ±0.01
2m	0.97 ±0.01	0.00 ±0.02	5.10 ±0.01

Similar situation can be observed Figure 30 and Figure 31, where the transmitter has been moved up to z=15 m, and the estimates using the receivers positioned at z=0.5 cm (Figure 30) and z=2 m (Figure 31) are compared. For the lower receiver position, the grid points closest to the target suffer enough field perturbation to provide wrong transmitter localization up to 4 m. For the higher receiver position, however (z=2 m), the field perturbations decay significantly, and all the receivers provide reliable transmitter location estimation within 25 cm accuracy (Figure 31, although the variation of the estimates by individual receivers are within only 1 cm from each other).

Finally, Figure 32 and Figure 33 show the estimates of the higher transmitter location (z=20 m) at the frequencies of 50 Hz and 200 Hz respectively. The receiver coil is fixed at z=2 m in both cases. First of all, compared to the previous case of the lower position (Figure 31), the 50 Hz transmitter is localized with less accuracy: z = 19.14 m, instead of the real value of 20 m. For the higher frequency, the error becomes much more noticeable: the estimated z = 15.94. This error growth can be attributed to the violation of our assumption of rot(H) = 0 for during the HAP matrix creation. The actual measurement of the magnetic field gradient in z direction, however, will help avoid this assumption and can possibly improve position estimation of distant sources at higher frequencies, provided the magnetic fields are still detectable.

Figure 34 and Figure 35 show the transmitter location estimation in the case when the scattering object is a large spheroid (diameter of 15 cm, length 60 cm), at two receiver elevations of z=50 cm and z=1 m respectively. As in the case of the sphere, the perturbation of the positioning by the spheroid is high for the receiver grid points closest to the object, however they decay significantly when the receiver is moved away from the object (Figure 35). Figure 36 illustrates that the magnetic field derivatives calculated using wider separation between the magnetic field measurements, can still provide accurate estimates for the HAP method. Compared to the data on Figure 35, the extracted transmitter z-position based on the primary field changed from 5.08 to 5.10 m, while that based on the total field – from 5.07 m to 5.09 m.

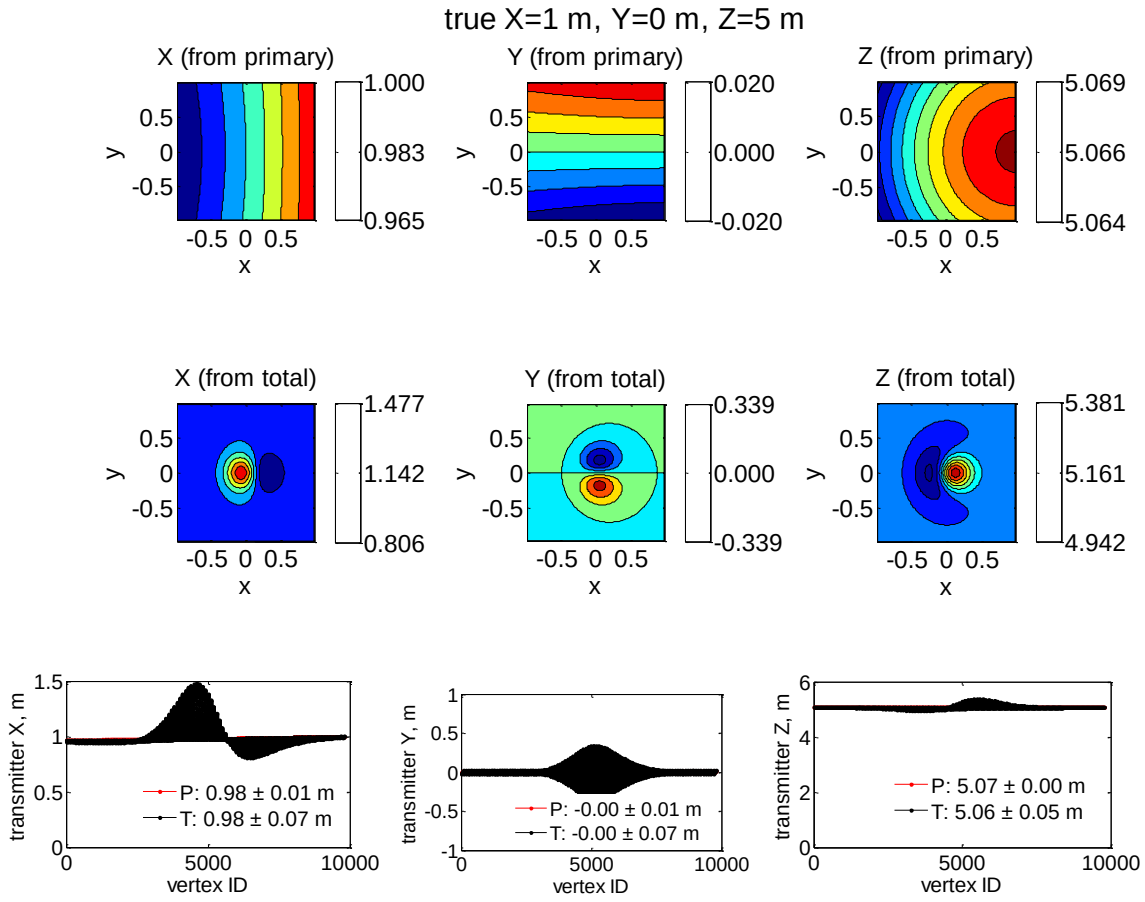

Figure 27. Sphere, D=0.1 m. Transmitter Z = 5 m. Frequency = 50 Hz. Receivers at z=0.5 m: Estimated transmitter coordinates (x, y and z) as functions of observation point (across the horizontal receiver). The top row corresponds to coordinates estimated from the primary magnetic field, the second row uses the total (primary+scattered) fields, while the bottom plots show the 2D expansion of the sensor array.

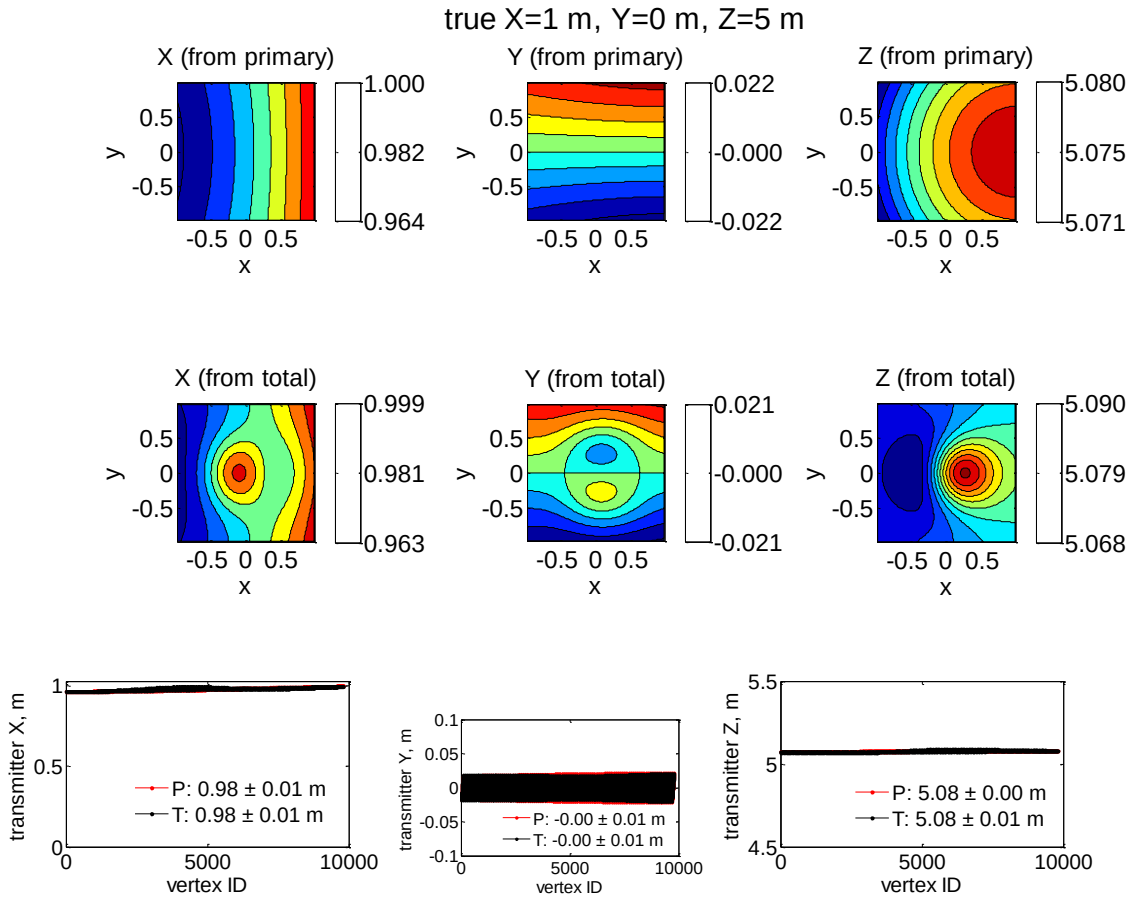

Figure 28. Sphere, D=0.1 m. Transmitter Z = 5 m. Frequency = 50 Hz. Receivers at z=1 m: Estimated transmitter coordinates (x, y and z) as functions of observation point (across the horizontal receiver). The top row corresponds to coordinates estimated from the primary magnetic field, the second row uses the total (primary+scattered) fields, while the bottom plots show the 2D expansion of the sensor array.

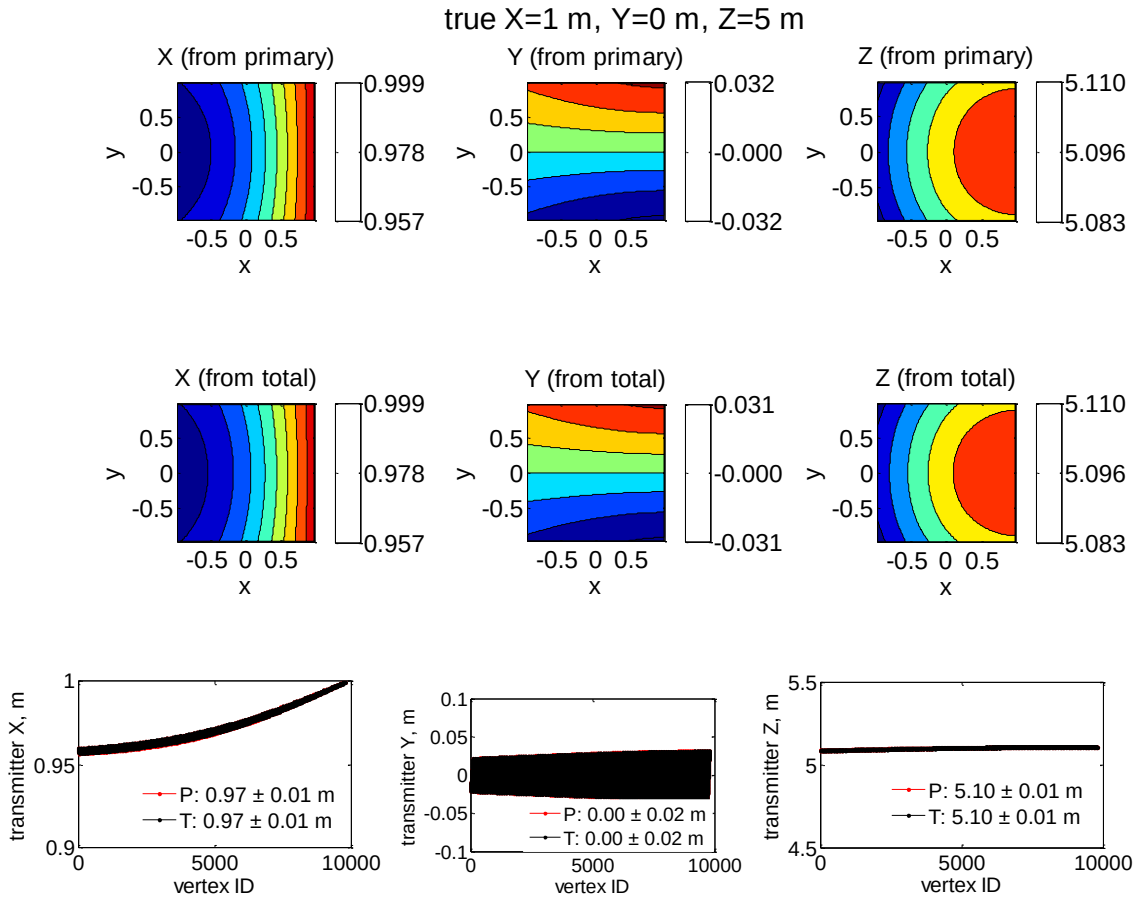

Figure 29. Sphere, D=0.1 m. Transmitter Z = 5 m. Frequency = 50 Hz. Receivers at z=2 m: Estimated transmitter coordinates (x, y and z) as functions of observation point (across the horizontal receiver). The top row corresponds to coordinates estimated from the primary magnetic field, the second row uses the total (primary+scattered) fields, while the bottom plots show the 2D expansion of the sensor array.

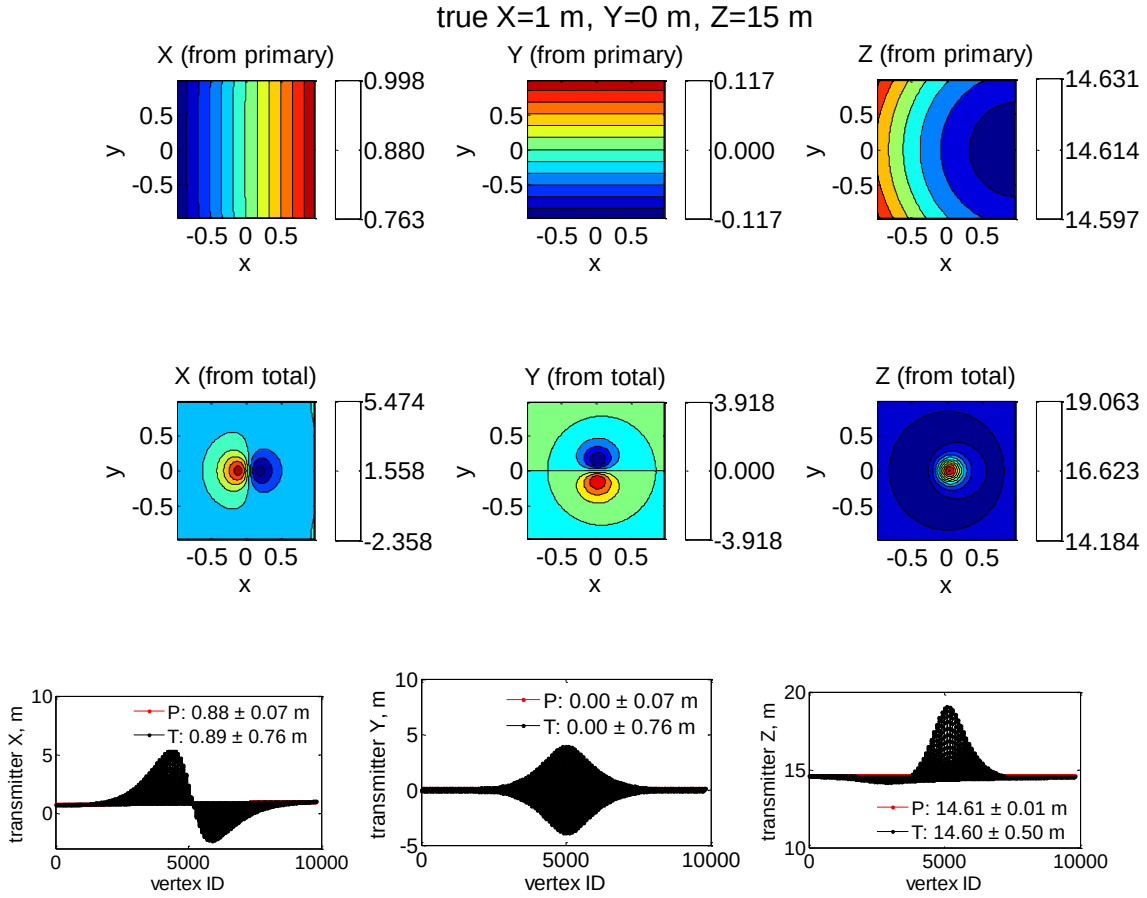

Figure 30. Sphere, D=0.1 m. Transmitter Z = 15 m. Frequency = 50 Hz. Receivers at z=0.5 m: estimated transmitter coordinates (x, y and z) as functions of observation point (across the horizontal receiver). The top row corresponds to coordinates estimated from the primary magnetic field, the second row uses the total (primary+scattered) fields, while the bottom plots show the 2D expansion of the sensor array.

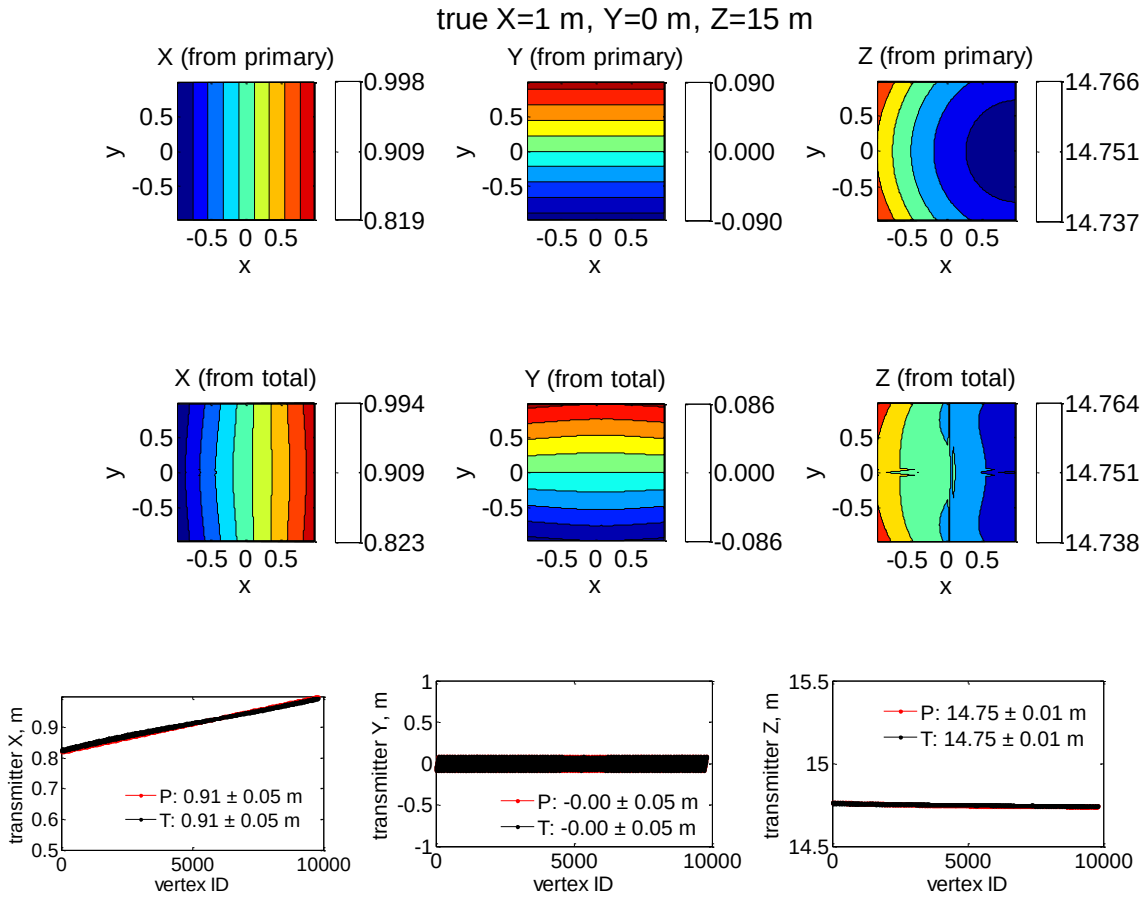

Figure 31. Sphere, D=0.1 m. Transmitter Z = 15 m. Frequency = 50 Hz. Receivers at z=2 m: Estimated transmitter coordinates (x, y and z) as functions of observation point (across the horizontal receiver). The top row corresponds to coordinates estimated from the primary magnetic field, the second row uses the total (primary+scattered) fields, while the bottom plots show the 2D expansion of the sensor array.

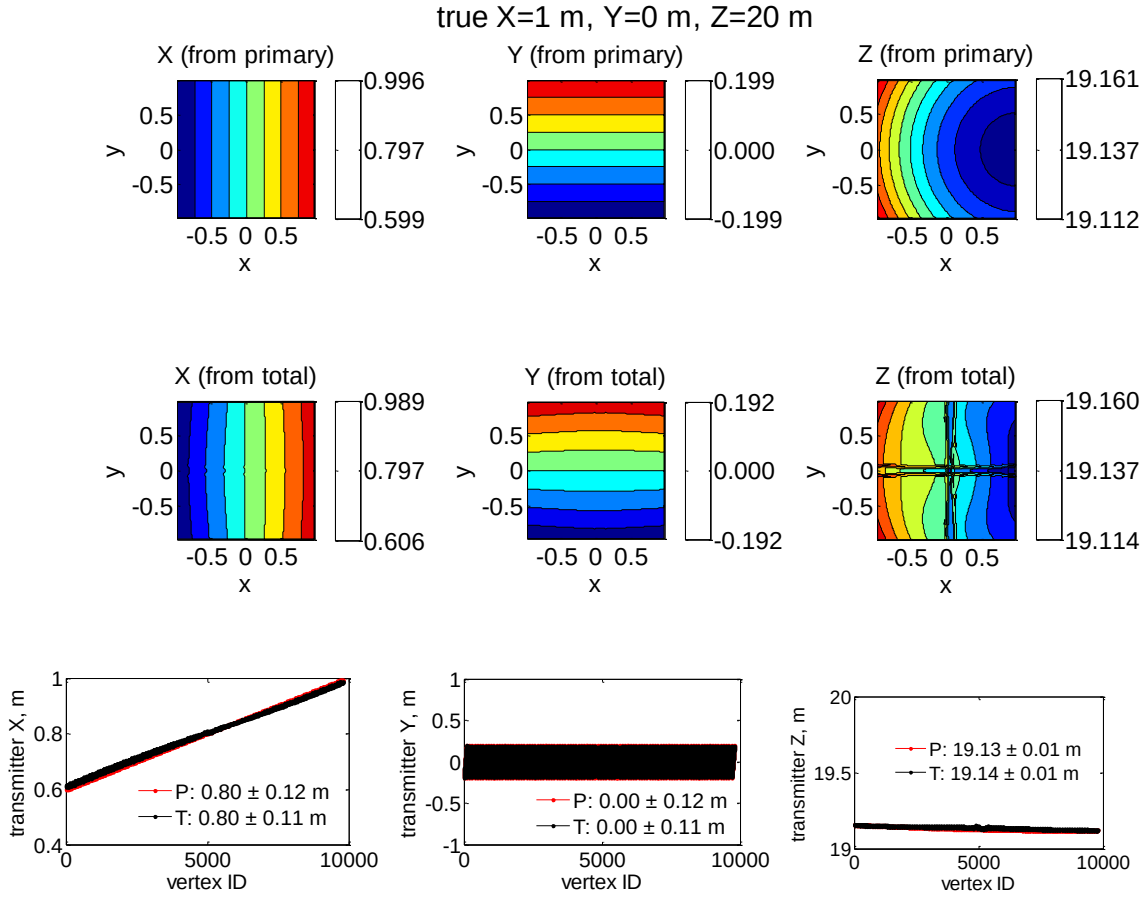

Figure 32. Sphere, D=0.1 m. Transmitter Z = 20 m. Frequency = 50 Hz. Receivers at z=2 m: Estimated transmitter coordinates (x, y and z) as functions of observation point (across the horizontal receiver). The top row corresponds to coordinates estimated from the primary magnetic field, the second row uses the total (primary+scattered) fields, while the bottom plots show the 2D expansion of the sensor array.

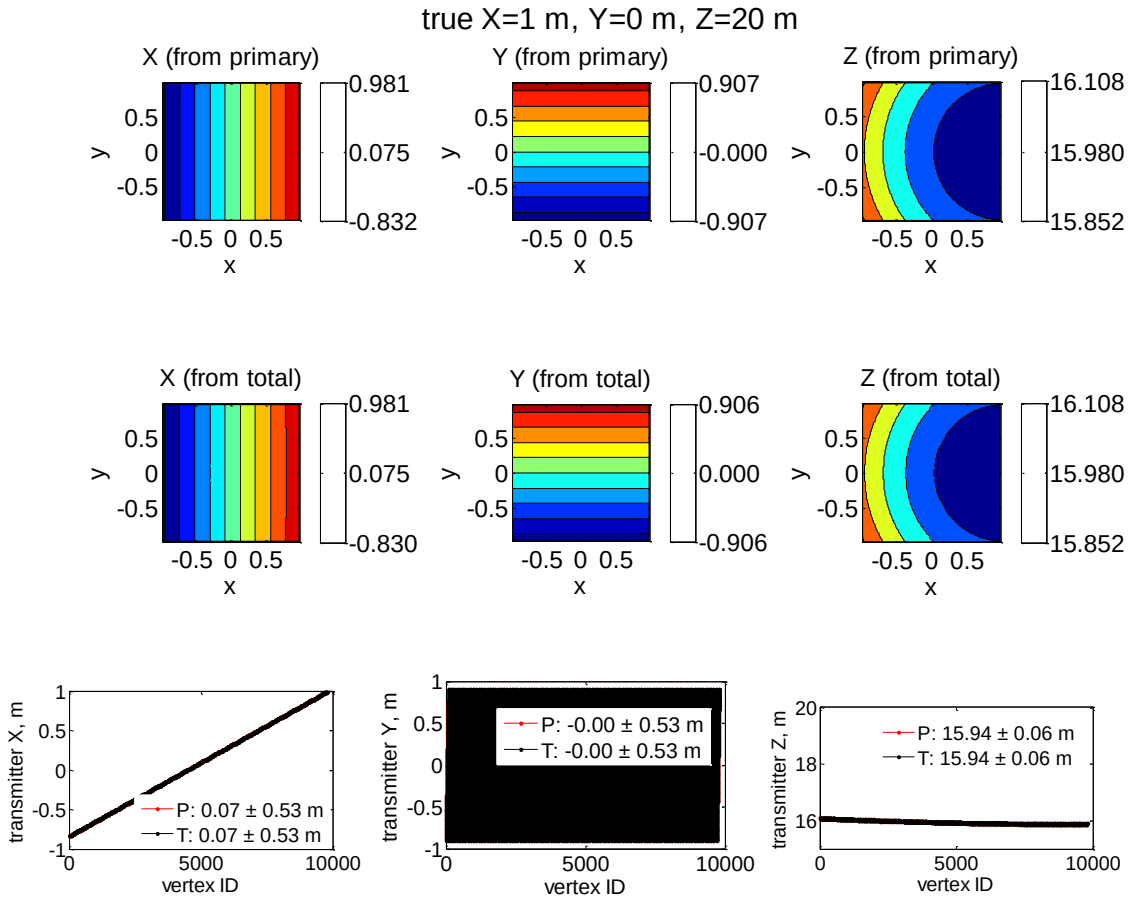

Figure 33. Sphere, D=0.1 m. Transmitter Z = 20 m. Frequency = 200 Hz. Receivers at z=2 m: estimated transmitter coordinates (x, y and z) as functions of observation point (across the horizontal receiver). The top row corresponds to coordinates estimated from the primary magnetic field, the second row uses the total (primary+scattered) fields, while the bottom plots show the 2D expansion of the sensor array. For higher frequencies the error grows.

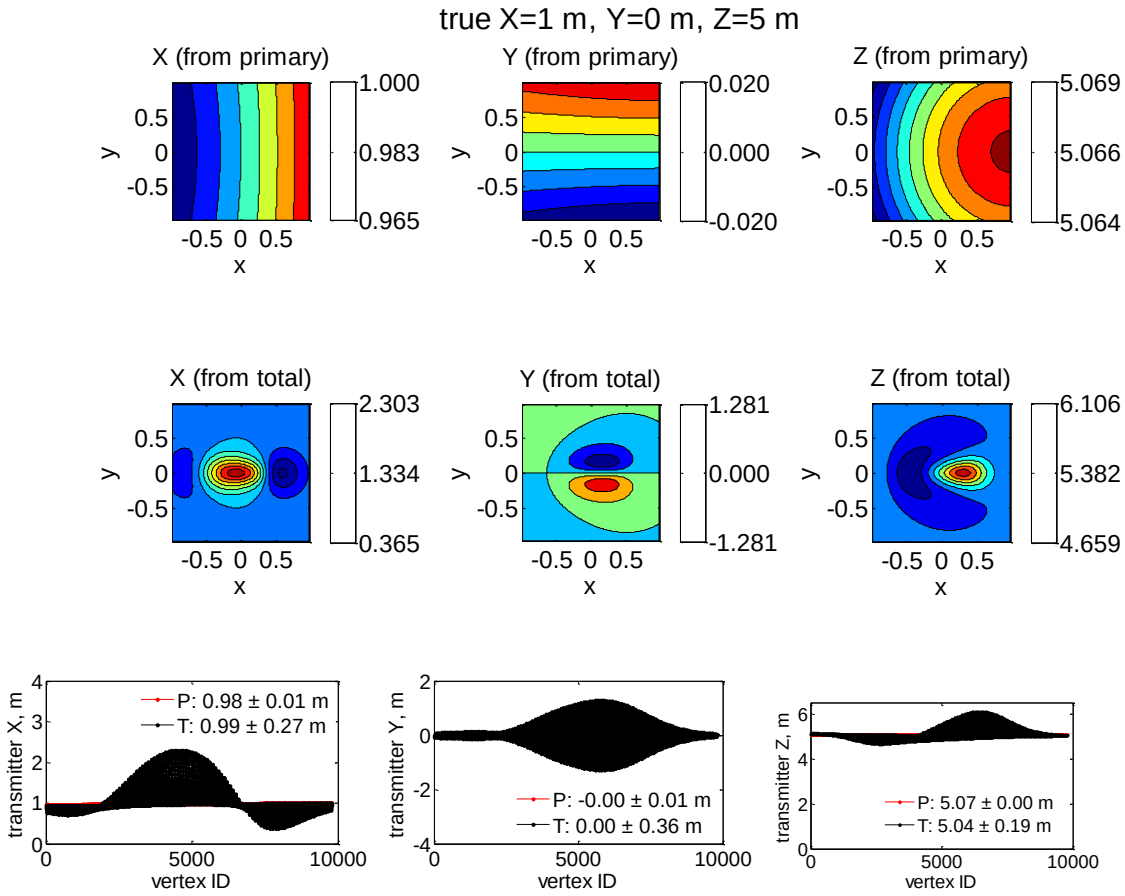

Figure 34. Horizontal Spheroid, D=0.15 m (aspect 4). Transmitter Z = 5 m. Frequency = 50 Hz. Receivers at z=0.5 m. Estimated transmitter coordinates (x, y and z) as functions of observation point (across the horizontal receiver). The top row corresponds to coordinates estimated from the primary magnetic field, the second row uses the total (primary+scattered) fields, while the bottom plots show the 2D expansion of the sensor array.

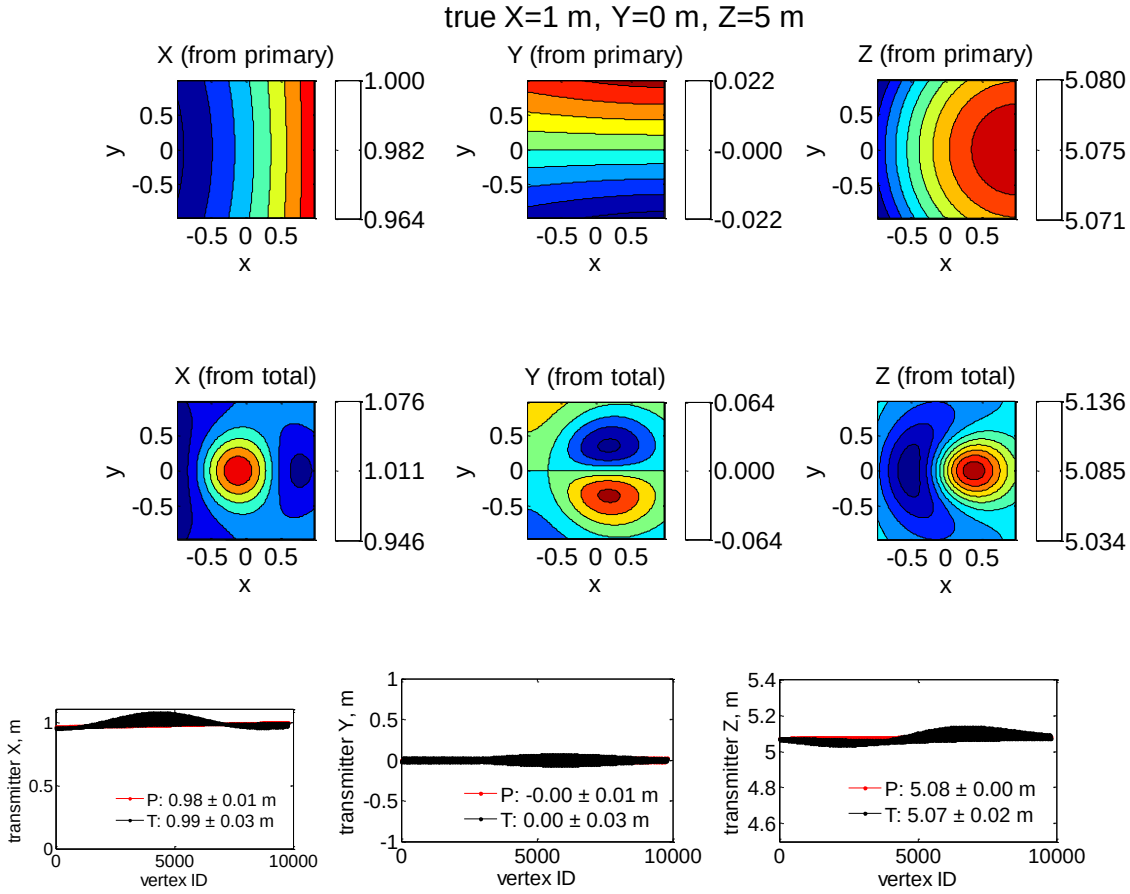

Figure 35. Horizontal Spheroid, D=0.15 m (aspect 4). Transmitter Z = 5 m. Frequency = 50 Hz. Receivers at z=1 m: Estimated transmitter coordinates (x, y and z) as functions of observation point (across the horizontal receiver). The top row corresponds to coordinates estimated from the primary magnetic field, the second row uses the total (primary+scattered) fields, while the bottom plots show the 2D expansion of the sensor array.

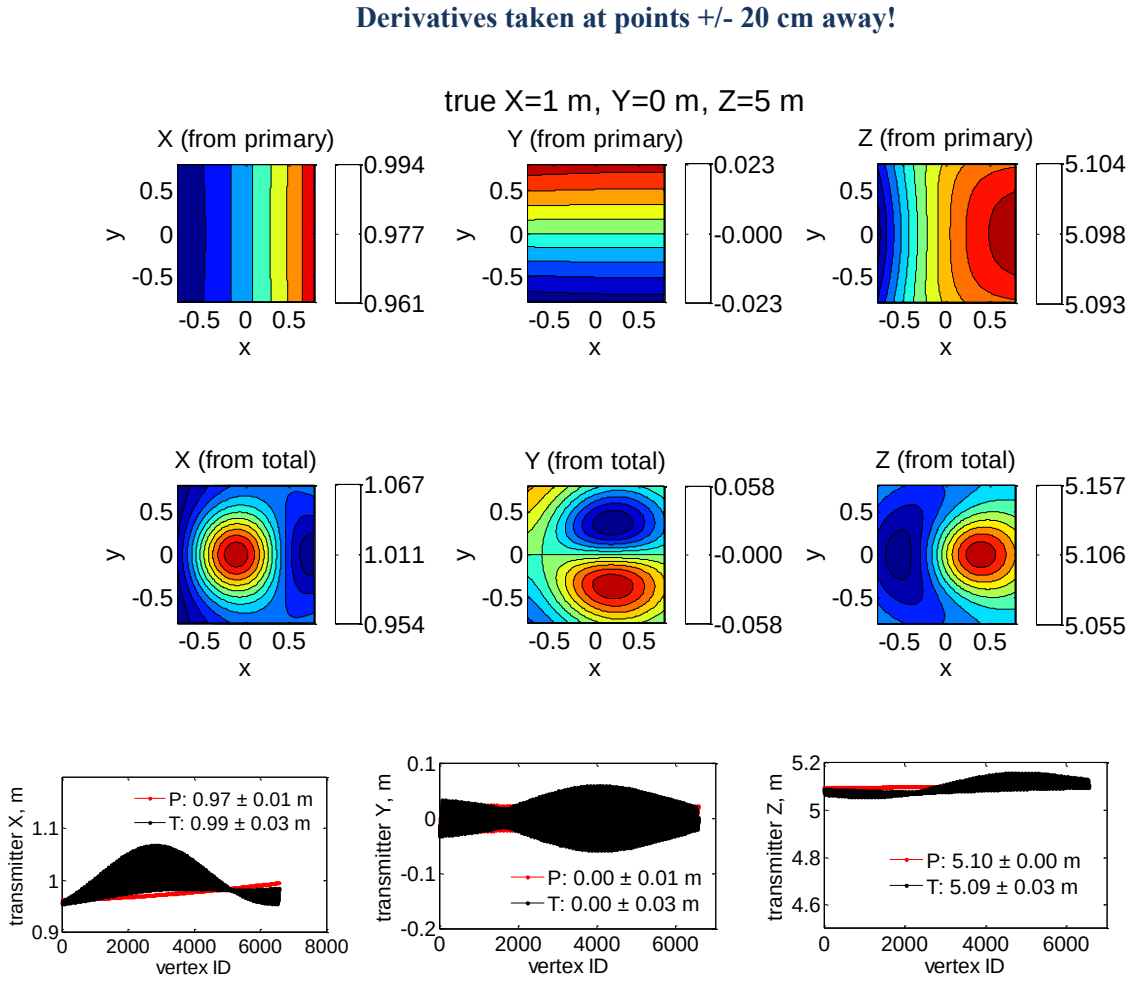

Figure 36. Horizontal Spheroid, D=0.15 m (aspect 4). Transmitter Z = 5 m. Frequency = 50 Hz.Receivers at z=1 m:Estimated transmitter coordinates (x, y and z) as functions of observation point (across the horizontal receiver). The top row corresponds to coordinates estimated from the primary magnetic field, the second row uses the total (primary+scattered) fields, while the bottom plots show the 2D expansion of the sensor array.

3.5 Determining Geo-location using non linear optimization algorithm

We have demonstrated that the closed form solution (2.10) provides reasonably good estimation of underwater geo-locations when there are relative large distances between Tx and Rx sensors. However, underwater UXO detection, and more importantly discrimination, requires centimeter-level accurate Geo-location even when the Tx are close to the Rx sensors. In addition, from cost savings point of view, it is desirable to have system with few Rx sensors. To achieve these goals, we investigated underwater geo-location accuracy using three vector Rx cubes Figure 37. The geo-locations are estimated using a non-linear inversion technique based on the DE technique.

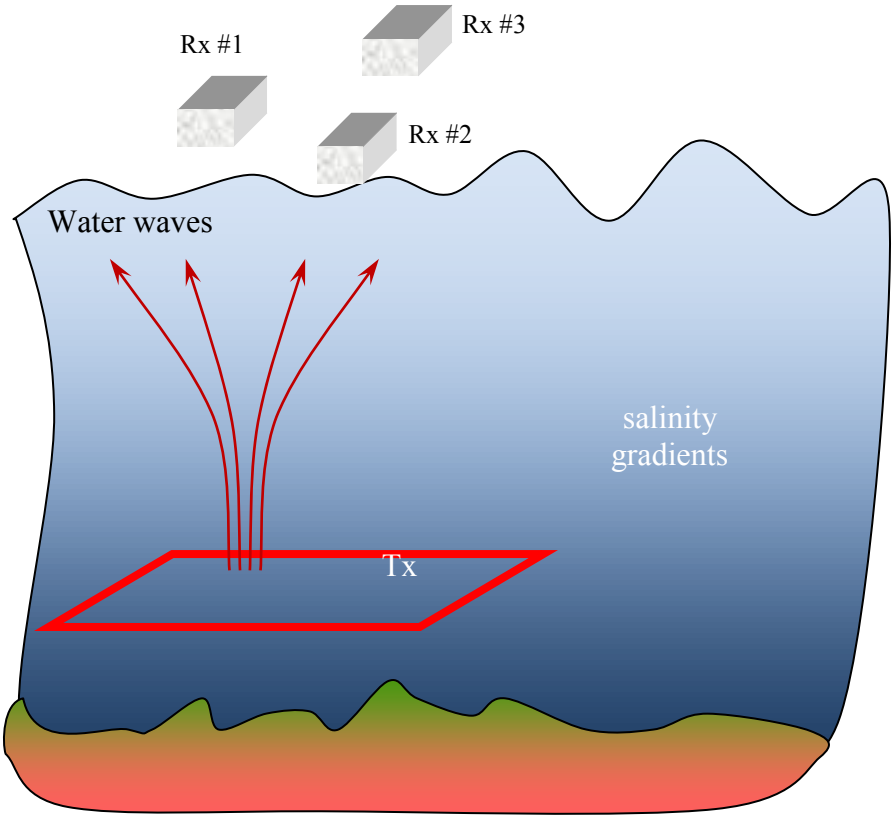

Figure 37. Geometry of a modified underwater geo-location system: the system consists one Tx and three vector Rx cubes. The Rx cubes are placed at the same plane and separated by the equal distances.

In the non-linear optimization technique, we considered two models for representing the primary magnetic field: 1) the modeled primary magnetic field is independent of frequency and of the Tx coils and surrounding medium's conductivity and 2) The modeled field depends on conductivity and frequency, the conductivity of the medium is given. From a practical implementation point of view, the first approach is more attractive since it does not require prior knowledge of the surrounding medium's conductivity, which in general is a function of salinity, temperature, and depth.

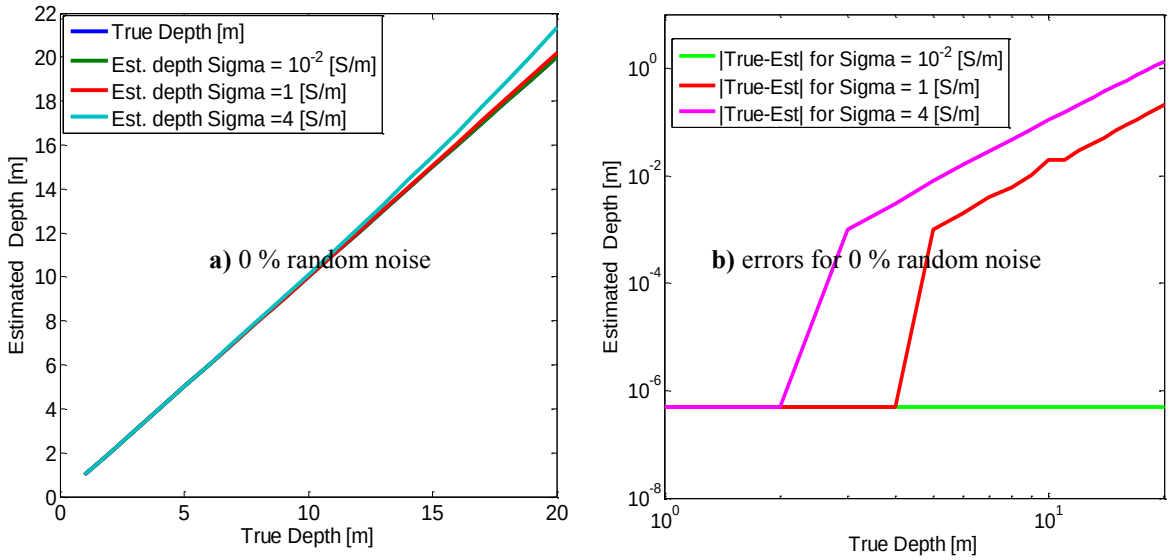

Figure 38. A) True and estimated depth of a underwater geo-location system for different conductivities. The results are obtained using the DE approach and the forward model that is independent on the conductivity. b) Absolute differences between the true and estimated values.

First we investigated applicability and limitation of the first approach (i.e. the model is independent of the conductivities). For these studies we generated synthetic data sets. We assumed that the Tx is placed in a uniform medium with conductivity a) $\sigma=10^{-2}$ [S/m], b) $\sigma=1$ [S/m] c) $\sigma=4$ [S/m]. Note that the code for generating synthetic data does not make any assumptions about the frequency or conductivity. All subsequent studies were done using 100 Hz frequency. We used three vector Rx cubic sensors. For determining the limitations of the proposed system performance we added random noise to each component of the Rx vector magnetic field. The system's geo-locations are determined using three vector receivers and non-linear optimization technique. The results are shown on Figure 38 for no random noise added and Figure 39 shows results for 1 %, 5 % and 10 % added random noise. The results clearly illustrate that for low conducting medium ($\sigma=10^{-2}$ [S/m], b) $\sigma=1$ [S/m]) the non-linear optimization technique provides centimeter-level accuracy up to 12 meters. Even for $\sigma=4$ [S/m] conducting background the method provides estimated depth within few cm accuracy for 10 % random added noise up to 10 meters. Thus the technique provides desirable centimeter-level accuracy for UW geo-location.

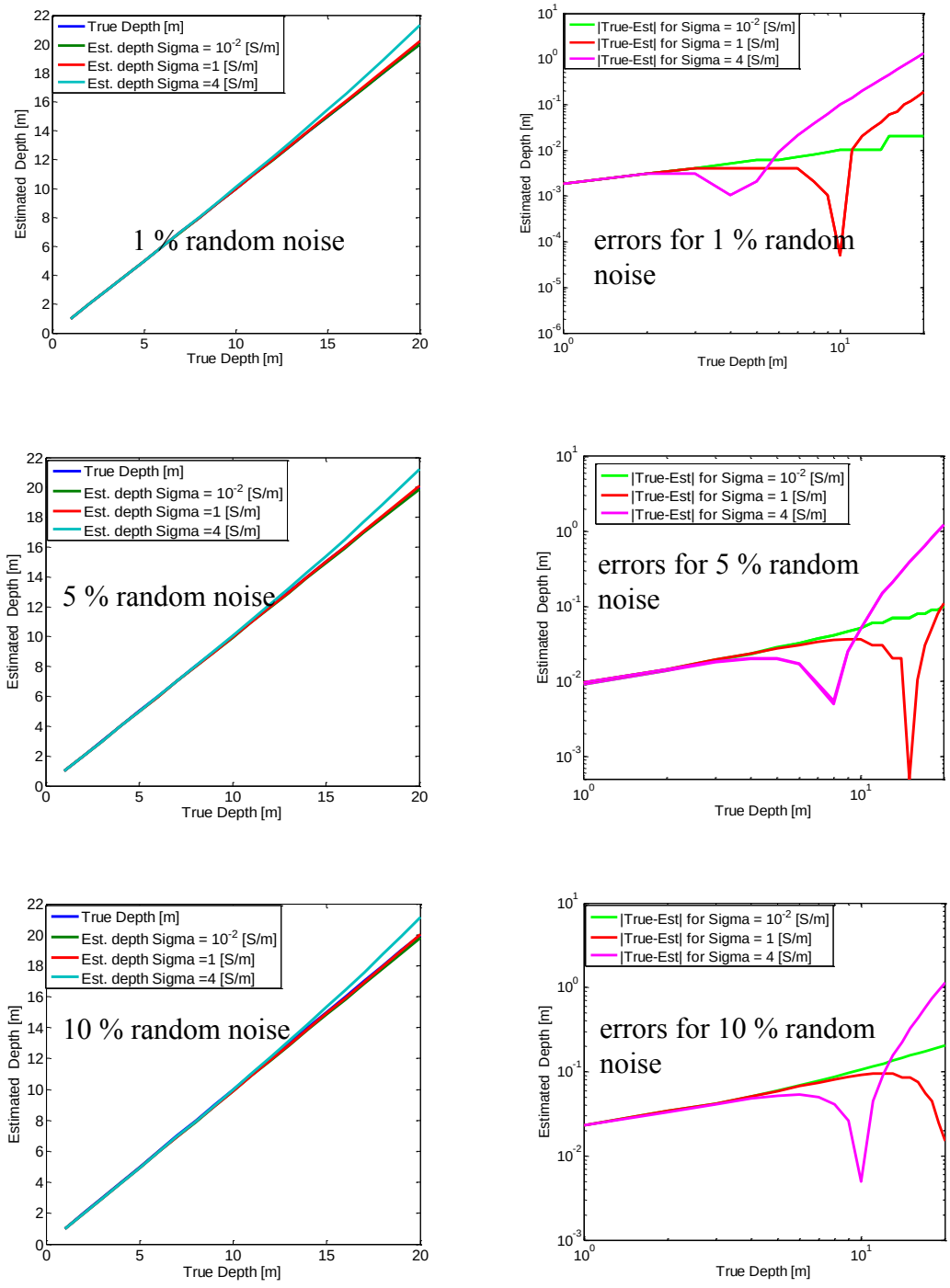

Figure 39. Left column: True and estimated depth of an underwater geo-location system for different conductivities and random noise levels. The results are obtained using the DE approach and the forward model that is independent on the conductivity. Right column: Absolute differences between the true and estimated values.

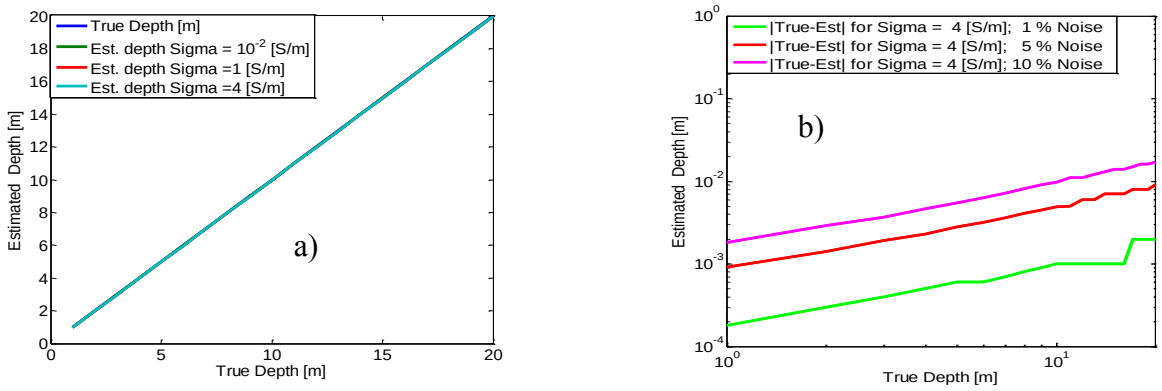

Figure 40. The results are obtained using the DE approach and the forward model that depends on the conductivity. a): True and estimated depth of a underwater geo-location system for different conductivities. b: Absolute differences between the true and estimated values.

Then, we assume that the conductivity of the medium is given and used this knowledge into forward model. We investigated accuracy of the DE and full forward model (i.e. model that depends on conductivity) for estimating underwater geo-location. The true and estimated depths are depicted on Figure 40. These results show that in the case when conductivity is known, the DE and full forward model provides centimeter-level accuracy for 4 [S/m] conducting medium even for the case with 10 % randomly added noise. Thus the three receiver system with non-linear optimization and full forward model provide desirable centimeter-level accuracy for underwater geo-location.

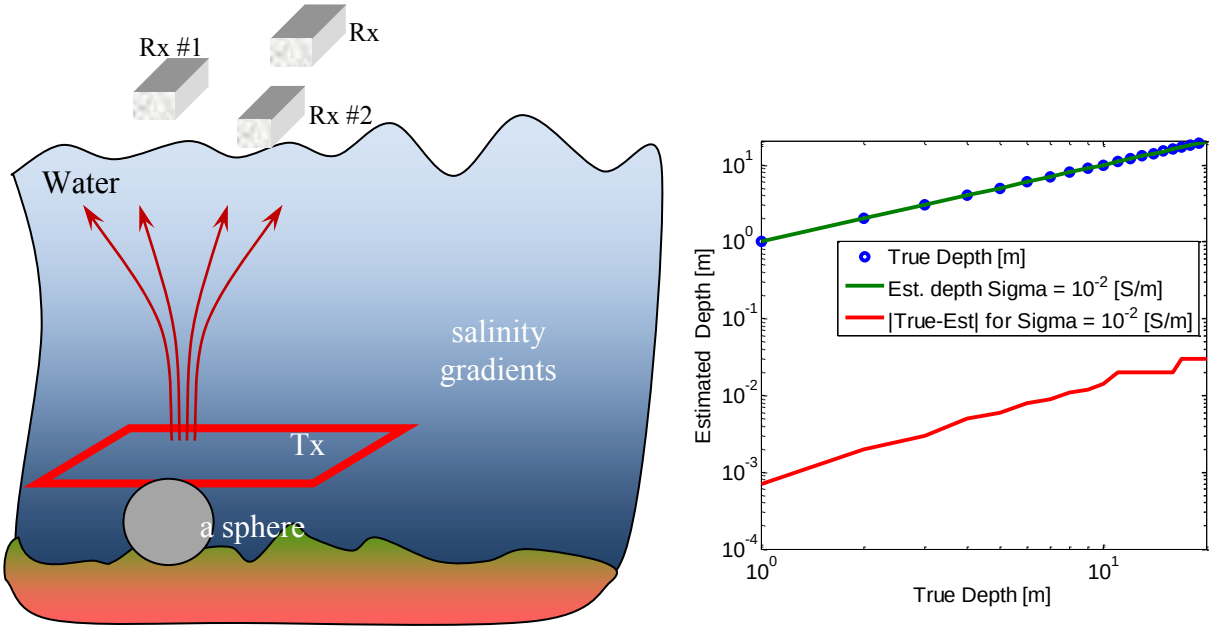

Figure 41: Left: A modified underwater geo-location system is placed above a metallic sphere, whit radius 15 cm, σ=4 10^6 [S/m] and permeability μ=100 [S/m]. Right: estimated and true depth for different random noise.

Finally, we assessed the system's performance when a high conducting and permeable metallic target is in Tx close proximity. The results are depicted on Figure 41. In this studies, Tx coil is placed 50 cm above a metallic sphere, with radius 15 cm , conductivity $\sigma=4\ 10^6$ [S/m] and permeability $\mu=100$ [S/m] and three vector Rx are placed at different elevations from the sphere's center. We assumed that all Tx, Rx sensors and sphere are placed inside 4 [S/m] conductive host medium. The estimated depth for different conductive medium are given on Figure 41 As expected, the estimated depth is within cm level accuracy, even for 10 % added random noise.

4 EXPERIMENTAL SETUP AND VALIDATION STUDIES

In this chapter we describe the experimental setup we developed to evaluate the effects of sensor noise/sensitivity on localization accuracy, is described. The experimental setup comprises a large moment dipole transmitter, a current source, and a magnetic field gradient receiver array. Highest quality gradient estimates are achieved with three vector magnetometers equally spaced and aligned with each axis (centered difference measurement). A minimum of 5 vector field measurements was used to estimate the complete magnetic field gradient tensor (centered difference along two orthogonal axes). The transmitter current source produces a 50% duty cycle waveform at frequencies ranging from sub-Hertz to several kHz. Available hardware limited our receiver array to a 10 Hz sample rate, which required a transmitter frequency below 1 Hz.

4.1 Hardware

As part of the experimental effort, we conducted a number of laboratory and field tests to validate the feasibility of our approach. The objectives of the experimental component were to implement the localization methodology with data sets and to identify sources of potential localization accuracy errors resulting from hardware or operational design features (e.g., receiver drift, receiver non-orthogonality, etc.).

To implement the localization methodology, we used a set of commercially available fluxgate magnetometers to measure the magnetic field gradients associated with a magnetic dipole transmitter.

We selected the Applied Physics Systems 1540 3-axis fluxgate (Figure 42) as a suitable receiver for our experiments. These sensors are compact (~5" length x 1" diameter), are relatively inexpensive (~$2400), and provide 3-axis magnetic field measurements with a sub-nanoTesla (nT) noise floor. While they do not offer the low noise characteristics afforded by atomic total field magnetometers, we determined that they would provide sufficient insight into the operational capabilities of commercial fluxgate sensors.

Figure 42. Applied Physics Systems 1540 magnetometer (www.appliedphysics.com)

We fabricated a small moment (~2 Ampere-meter squared [A-m$^{2]}$) transmitter and a large moment (~2400 A-m^2) transmitter for laboratory and outdoor tests, respectively (Figure 43), to generate a sufficient source field for the receivers. The transmitter coils were fed by a Zonge International, Inc. ZT-30/XMT-32 transmitter/controller source (Figure 43.) with current levels ranging from 0.2 – 20 Amps. We selected a bipolar square wave at 50% duty cycle for the source waveform. This waveform enabled DC measurements of the transmitter-on/transmitter-off magnetic field to determine the source field strength.

Figure 43. Dipole transmitters. Small moment transmitter (LEFT) for indoor testing; large moment transmitter (CENTER) for outdoor testing; Zonge International, Inc. ZT-30 transmitter source and XMT-32 transmitter controller (RIGHT).

4.2 Data collection strategy for localization

The principles for implementing the localization methodology are derived from the basic localization relationship see equation (2.10). In the case of our source/receiver experimental setup, the localization relationship is applied to the source magnetic field vector and gradient tensor values measured at the receiver location. Figure 44. illustrates the localization concept applied to experimental measurements.

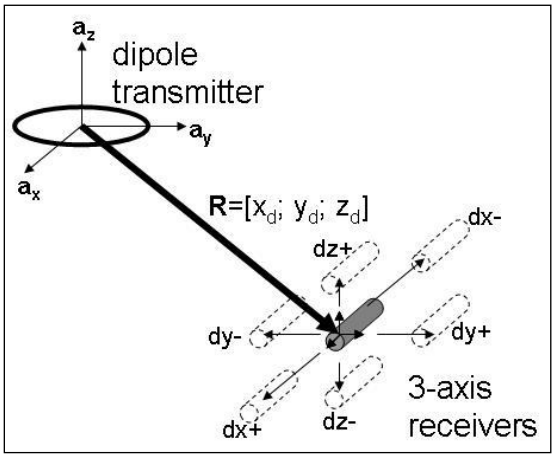

Figure 44. Experimental application of localization concept. Differential measurements of the source field produce gradient tensor elements and vector field values at the nominal receiver location. These values are used in the localization relationship to yield the nominal receiver position [$x_d\, y_d\, z_d$].

Figure 44. depicts application of center difference measurements along the three orthogonal sensor axes to determine the complete gradient tensor. The center difference method approximates each gradient in the tensor by measuring the difference in magnetic field values at two opposing locations that are equidistant from the nominal (center) location. In the limiting case where this offset from the center approaches zero, the center difference is equivalent to the gradient. Figure 45 shows a representation of the center difference method applied to our experimental setup.

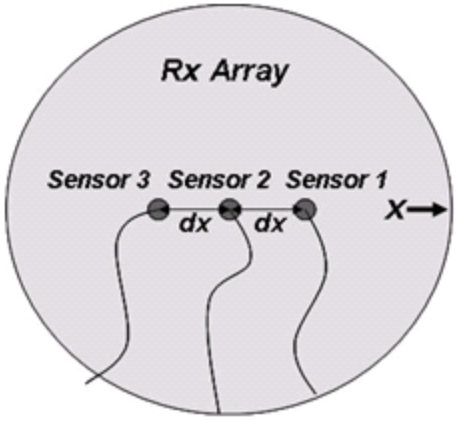

Figure 45. Receiver configuration for center difference approximations of the magnetic field gradients along the x-axis of the receiver array. The sensor offset is represented by the *dx* value.

Another gradient approximation may be implemented by using the magnetic field value difference between two sensors and then choosing one of the sensors for the nominal value. This single offset approach reduces the number of sensors required for each axis from 3 to 2; however, the quality of the approximation degrades more rapidly than the center difference method as the offset between sensors increases. Figure 46 shows the gradient approximation quality (in terms of the localization estimate) as a function of sensor offset for the two methods.

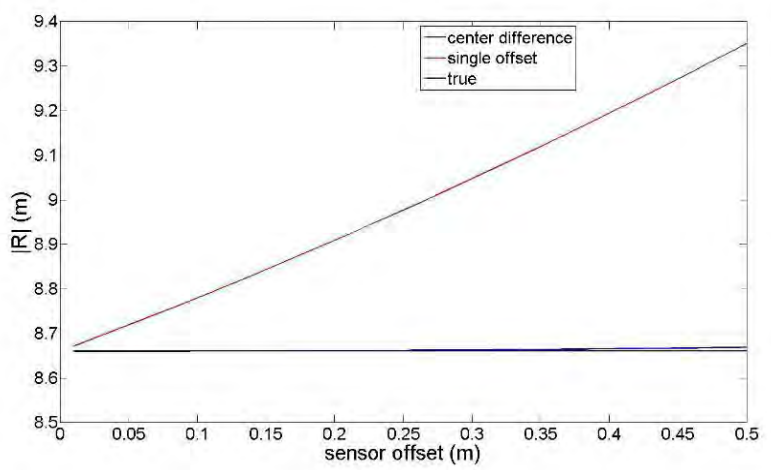

Figure 46. Localization estimates for center difference (blue line) approximation and single offset (red line) approximation compared to the true value (black line). The quality of the localization estimate obtained with the single offset approximation degrades much more rapidly with sensor offset when compared with the quality of the estimate obtained with the center difference method.

We may rewrite (2.10) using the magnetic field gradient tensor symmetry properties:

$$\begin{bmatrix} \frac{\partial B_x}{\partial x} & \frac{\partial B_y}{\partial x} & \frac{\partial B_z}{\partial x} \\ \frac{\partial B_x}{\partial y} & \frac{\partial B_y}{\partial y} & \frac{\partial B_z}{\partial y} \\ \frac{\partial B_z}{\partial x} & \frac{\partial Bz}{\partial y} & -\left(\frac{\partial B_x}{\partial x}+\frac{\partial B_y}{\partial y}\right) \end{bmatrix} \begin{matrix} x_d \\ y_d \\ z_d \end{matrix} \quad 3 \begin{matrix} B_x \\ B_y \\ B_z \end{matrix}$$

This expression requires measurement of gradients along only two orthogonal axes to complete the tensor. Applying this principle to our experimental measurements, we designed a planar test fixture to enable gradient measurements along two orthogonal axes using the 1540 magnetometers. Inherently, this configuration reduces the number of measurement points from 7 to 5 in order to obtain the tensor elements. In our experiments, we used 3 sensors to measure the gradient along a single axis and then repeated the measurements along the complementary axis. This minimized the number of sensors required for the data collection. Figure 47 shows the receiver test fixture.

Figure 47. Receiver test fixture. Three vector magnetometers measure the center difference gradient values along two orthogonal axes (LEFT, CENTER). The receiver array is placed at various offsets from the transmitter to obtain localization estimates (RIGHT).

4.3 Data collection and analysis

Using the aforementioned gradient configuration, we measured the magnetic field response in the 3 fluxgates located along each axis of the test fixture. By calculating a difference between the magnetic field response during the transmit-on period and the response during the transmit-off period we were able to isolate the source field components at each measurement location (Figure 48).

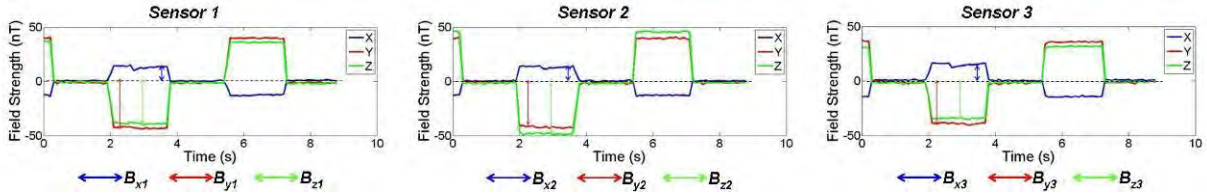

Figure 48. Raw magnetic field data recorded by the three 1540 magnetometer receivers. Source field values are determined by measuring the difference between the transmit-on values and the transmit-off values.

The design of the test fixture enabled placement of the receivers at a variety of offsets from the center point. Analytically, the center difference approximation provides higher quality estimates when the sensor offsets are very small (Figure 48); however, in practice the inherent noise characteristics of the sensor limit the effectiveness of small offsets. Figure 49 shows the results of adding noise (normalized to an effective 0.1 nT standard deviation) to simulated center difference measurements of the source field. For noisy data, the localization estimates improve with larger sensor offsets (to the extent that the noise induced errors are greater than the offset induced errors).

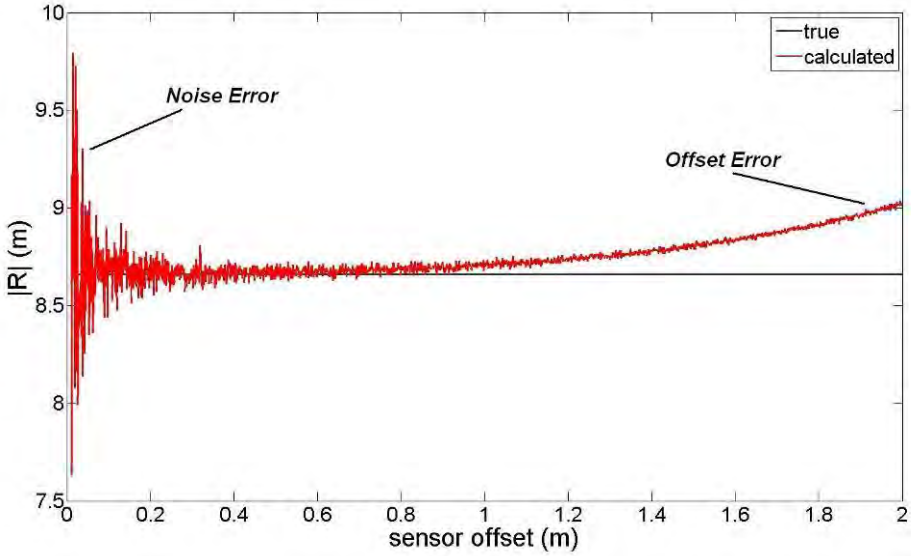

Figure 49. Localization estimate for simulated noisy data. Noise with standard deviation of 0.1 nT is added to magnetic field values associated with the transmitter source field. At small sensor offsets (<0.3 m), the error caused by the noise is much greater than error caused by the sensor offset. Even at the relatively large offset of 2 m, the offset induced error is still smaller than the noise induced error obtained at very close offsets (<0.1 m).

We evaluated the relationship between sensor noise and localization error for a set of locations between 0-25m from the dipole transmitter. Using the 1540 vector magnetometers, we were able to maintain ~0.5m accuracy at a range of 12m from the 2400 A-m^2 source. One of the key metrics in evaluating the localization capability of the receiver configuration is the comparison of the sensor noise floor to the magnetic field difference associated with the gradient estimate. We define this metric as the differential SNR:

$$\mathbf{SNR} = \frac{\sigma}{\left[\frac{1}{9}\sum_{\gamma}\sum_{\zeta}\left|\frac{\partial B_{\gamma}}{\partial \zeta}\right| d\zeta\right]} \qquad \gamma, \zeta \in \{x, y, z\}$$

where σ is the sensor noise standard deviation, $\frac{\partial B_{\gamma}}{\partial \zeta}$ represents a gradient tensor element, and $d\zeta$ represents the offset between the receivers. Figure 50 shows the localization error versus the differential SNR achieved in our experiments for 5 different |R| values.

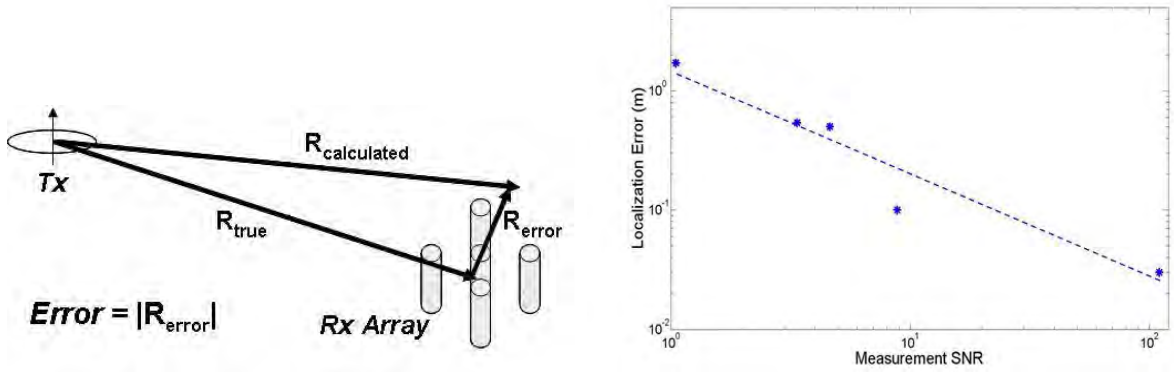

Figure 50. Localization error as a function of differential measurement SNR. These localization errors correspond to 5 measurements recorded within a range of 0 – 25 m from the transmitter source. A sensor offset of 15 cm was used for the receiver configuration.

Although the vector sensors could detect the transmitter field at ranges >40m, the magnetic field differential between the receivers was very small; much lower than the sensor noise floor. As a result of this low differential SNR, localization error increased to several meters.

In addition to noise induced error, it is likely that the inherent non-orthogonality of the sensors and small angle misalignment in the fixture contributed to the localization error (Figure 51). Small error angles (e.g., non-orthogonality or misalignment of axes) can produce relatively large inaccuracies (~ 1 m) in the position estimate when the receivers are located several meters from the transmitter source (Figure 51).

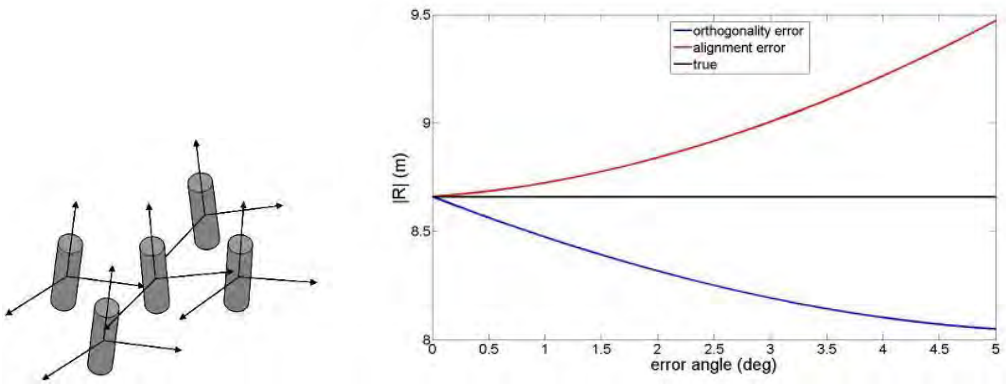

Figure 51. Inherent non-orthogonality of the sensor axes (LEFT) and misalignment of sensors in the receiver fixture (CENTER) can result in large errors in the localization estimate. The plot (RIGHT) shows localization estimate versus the error angle for separate cases of non-orthogonality (blue line) and sensor misalignment (red line).

Using a test fixture enhanced the accuracy of the relative sensor positions; however, the sensors were subjected to inherent non-orthogonality errors along the measurement axes, as well as some error in the alignment of the sensors resulting from the machine tolerances used in the fabrication of the fixture. For a prototype system, we anticipate that any non-orthogonality or misalignment could be accounted for by using a calibration routine to determine the error angles. For a complete array, measurement of the field produced by several sources of known strength at known positions would provide enough information to extract the values of these errors. Once the error angles are obtained, they would be used in the localization algorithms to produce a higher quality position estimate.

In addition to providing corrections for non-orthogonality and misalignment, there are a number of methods for improving localization accuracy relative to that achieved in our experiments. Specifically, the transmitter moment could be further increased with greater power levels (>200 W) and more coil windings to provide similar accuracy at increased range. It would be possible to increase the transmitter moment by an order of magnitude over that used in our experiment by increasing the current and using thicker gauge wire in the windings to accommodate the resulting thermal load. Additionally, localization accuracy could be improved by using multiple transmitters, or by incorporating higher sensitivity magnetometers. For example, some atomic magnetometers offer a 20X reduction in noise when compared to the low cost fluxgates used in our experiment (Figure 52).

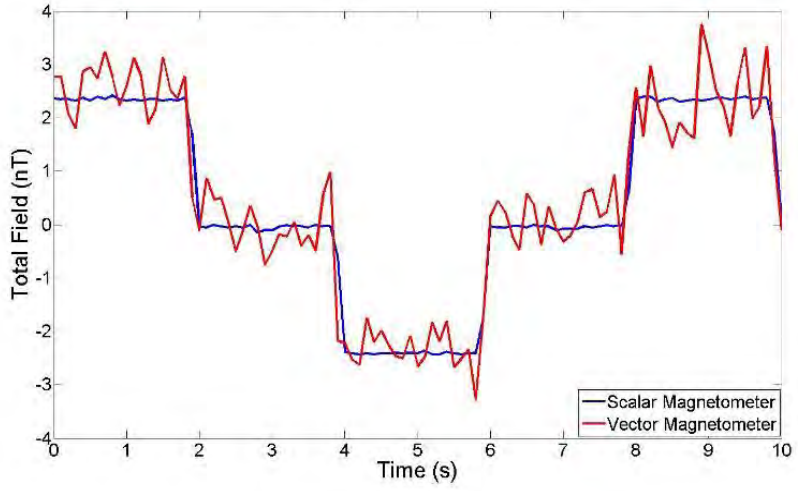

Figure 52. Magnetic field measurements taken at a distance of 40 m from the large moment transmitter. The vector magnetometer measurements (red line) were recorded with the Applied Physics Systems 1540 magnetometer; the scalar measurements (blue line) were recorded with the Geometrics G-823 atomic magnetometer. The atomic magnetometer offers a 20X reduction in noise.

Ultimately, we expect localization accuracy of better than one meter at a range of at least 40 m from the transmitter could be achieved by implementing a number of the aforementioned improvements in a prototype system.

5 DISCUSSION AND CONCLUSIONS

5.1 Objectives

The objective of this research project was to determine the feasibility of using low frequency electromagnetic positioning sensors for tracking the location of underwater interrogation sensors with centimeter-level accuracy. The proposed system's theoretical basis and hardware configurations are based on measurement of a low frequency vector magnetic field and its gradient. The specific technical objectives were the following:

1) Systematically investigate what configuration of an active DC magnetic field transmitter offers the optimal compromise between size, shape, and practical implementation for the maximum transmitter range in the UW environment for locating the transmitter with centimeter-level accuracy.
2) Optimize and design tri-axial receiver sensor configurations to accurately estimate geo-location by using non-linear optimization techniques and by approximating the tensor gradient of an actively transmitted DC magnetic field from the spatial differences between the receivers. The transmitted magnetic field and its gradient at the receiver locations provide sufficient data for locating and tracking underwater UXO sensors with respect to the surface GPS system.
3) Systematically investigate how noise sources, such as the air-water interface, will influence the proposed system's performance and establish the transmitter location precision and accuracy baseline under common noise levels.
4) Demonstrate the positional accuracy of the system by carrying out controlled measurements.

Under this project we utilized two methods for determining the location of underwater interrogation sensors with centimeter-level accuracy. (a) the vector magnetic field full tensor gradient based approaches and 2) a non-linear optimization, namely the DE approach. We assessed the ability of each technique to predict the location of an underwater interrogation system by comparing estimated results to the ground truth. The studies were done for different water conductivities, Tx geometry, and operating frequencies. We found that for realistic water conductivities, the frequency should be less than 100 Hz. This is due to the EM absorption in a conducting medium. In addition our studies showed that as the medium's conductivity increases the proposed system's performance degrades. Since in a low frequency EMI regime the primary field depends on the conductivity in the same form as the frequency, the problems related to the high conductivity can be overcome by reducing the frequency.

We illustrated that both magnetic field full tensor gradient and DE techniques have the potential to determine underwater geo-location. However, when the primary magnetic field signals are contaminated with random noise due to underwater metallic targets, water conductivity/frequency changes, and transmitter size, the performance of the vector magnetic field full tensor gradient approach degrades significantly compared to that of the non-linear optimization technique i.e. DE method. In addition, the number of Rx required by the vector

magnetic field tensor gradient technique and its sensitivity with respect to sensor separations prevented us from further considering this technique for UW geo-location, leaving the non-linear approach that uses only three vector Rx, as our technique of choice for tracking the location of underwater interrogation sensors with centimeter-level accuracy.

5.2 Optimal forward model selection for estimating UW Geo-location

Determining underwater geo-location with centimeter-level accuracy using a low frequency magnetic field requires a solution using a non-linear optimization technique. The technique builds an objective function, which is misfit between the measured data and modeled data. In these studies we considered two forward models for estimating UW Geo-location using the non-linear optimization technique, namely the DE. The DE is a heuristic, parallel, direct-search method for minimizing nonlinear functions of continuous variables. It is similar in concept to the genetic algorithm as applied to discrete variables. It is very easy to implement and has good convergence properties. The entire DE optimization process can be divided into four steps. The first step creates random initial populations that span the entire parameter space. The second step is the calculation of the primary magnetic field for all of the population. The third step is evaluation of the cost function, and the fourth step is storing the best parameters. By examining and sorting the cost function at each step, the best half of the population is chosen as the next generation's parameters, whereas the bottom half is discarded. Thereafter the next generation is created by crossing over and mutating the parameters in the previous generation. This process is repeated until the maximum number of generations has been reached or until a desirable objective function is found. Thus the crucial part for a non-linear optimization always is the forward model.

In a conducting environment the low frequency magnetic field depends on the conductivity. For a fixed frequency, this dependence increases as the separation between the transmitters and receivers increases. Thus, for determining the Rx sensors UW geo-location respect to Tx requires the water's conductivity. Since the conductivity is a function of water temperature and salinity, determining its values during geophysical data collection would not be an easy task. To overcome this challenge we assessed the feasibility of using a conductivity/frequency independent forward magnetic field model and compared its performance to the model that includes the water's conductivity. Our studies showed that the conductivity independent model provides centimeter-level accuracy up to 10 meters (30 feet) using one transmitter and three vector Rx sensors. This distance can be doubled by deploying additional Tx, or can be tripled by using two transmitters and two sets of three vector Rx sensors, and etc.

5.3 Optimal Tx and tri-axial *Rx* sensor configurations

We conducted a thorough numerical investigation for determining the best Tx and Rx configurations. We investigated how underwater highly conducting metallic objects change on the proposed system performance. We demonstrated that in cases when Rx sensors are close to a metallic target, then the secondary magnetic field due to the UW metallic target produces secondary magnetic field that in some cases is comparable to the primary magnetic field. This significantly degrades the system's performance for UW geo-location. To overcome this problem, based on the thorough studies, we concluded that the position of the Tx and Rx sensors should be reversed, namely the Tx should be close to the targets and Rx sensors should far from

metallic targets i.e. should be placed above the Tx. Our studies also showed that three Rx sensors placed on the same plane with equal separation is the Rx sensors' optimal configuration.

5.4 Outlook

Using our numerical tools, we successfully demonstrated that the low frequency magnetic field positioning sensor system has great potential for tracking the location of underwater interrogation sensors with centimeter-level accuracy. We illustrated the system's advantages and limitations, and provided the Tx and Rx sensors optimal design. However, in order to take full advantage of this an inexpensive, under water geo-location system, with centimeter-level accuracy, substantial hardware system integration and a thorough data analysis effort must be undertaken before the technique can be applied to real-world underwater UXO problems. This effort should address, among others, the following issues:

- **Building an underwater deployable Tx transmitter:** Under this project we built a 2x2 transmitter, and successfully measured the magnetic field. However, to deploy the system in the underwater environment, significant modifications /adjustments are needed, such the all electronics must be waterproof, the deployment strategies need to be determined, etc. Since one of the emerging technologies for under water UXO detection and discrimination is EMI sensing, we would expect that the existing active EMI systems can be employed as a potential Tx. We would expect that, this system will provide enough primary field for geo-location, particularly in case of shallow (<10 m) water.

- **Building a Tx-Rx combination for deep underwater Geo-location:** We showed that a single Tx and three vector Rx sensor allows us to achieve centimeter-level accuracy up to 10 meter depth. This depth can be increased further by inserting Rx into water and adding one more Tx above the Rx-s. Combining the different numbers of Tx and three vector Rx-s sensor sets, one can operate at any desirable depth. In order to demonstrate this capability a Tx and Rx chain should be built and its practical applicability for underwater geo-location investigated.

6 REFERENCES

1.SERDP, 2006, SERDP&ESTCP Workshop on Technology Needs for the Characterization, Management, and Remediation of Military Munitions in Underwater Environments.

2.Steven A. Arcone, "Ground-Penetrating Radar Survey of Subbottom Munitions in a Small New England Lake", *in* Proceedings Partners in Environmental Technology Technical Symposium & Workshop, Washington DC, November 2006.

3.Jim McDonald, "UXO Detection and Characterization in the Marine Environment" *in p*roceedings Partners in Environmental Technology Technical Symposium & Workshop, Washington DC, November.

4.Delaney, W. P. and Etter, D., 2003, Report of the Defense Science Board on unexploded ordnance: Office of the Undersecretary of Defense for Acquisition, Technology and Logistics, December 2003.

5.Schultz, G., Foley, J., Glenn, T., and I. Monteith, 2009, MM-1631 Underwater ordnance characterization using AUV technology, Proc. of the SERDP & ESTCP Partners Symposium, Washington DC.

6. Norton, S.J.; SanFilipo, W.A.; Won, I.J.; "Eddy-current and current-channeling response to spheroidal anomalies". GeoScience and Remote Sensing, IEEE Trans. vol. 43, Issue 10, Oct. 2005 pp:2200 – 2209.

7. Shubitidze, F., Shamatava, I., Fernandez, J.P., and B. Barrowes, 2009, MM-1632 Modeling EMI scattering phenomena in a conducting environment to enhance under water UXO detection and discrimination**,** Proc. of the SERDP & ESTCP Partners Symposium, Washington DC.

8. Shubitidze, F.. SERDP –SEED MM-1592 Final report. September 2008.

9.F. Shubitidze, K. O'Neill, S.A. Haider, K. Sun, and K.D. Paulsen, "Application of the method of auxiliary sources to the wideband electromagnetic induction problem," *IEEE Trans. Geoscience and Remote Sensing*, 40(4), 928–942, April 2002.

10. Shubitidze F., O'Neill K., Sun K., Shamatava I., and Paulsen K., 2004, "A hybrid full MAS and combined MAS/TSA algorithm for electromagnetic induction sensing", Journal of Applied Computational Electromagnetic Society, 19 b, pp. 112-125.

11. Shubitidze F., O'Neill K., Shamatava I., Sun K., and Paulsen K, 2004, A fast and accurate representation of physically complete EMI response by a heterogeneous object, IEEE Transactions on Geoscience and Remote Sensing, Volume 8, pp 1151-1162.

12. . Grant and G.West*, Interpretation Theory in Applied Geophysics*. New York: McGraw-Hill, 1965, pp. 306–381.

13. S. V. Marshall, "Vehicle detection using a magnetic field sensor," *IEEE Trans. Veh. Technol.*, vol. VT-27, no. 2, pp. 65–68, May 1978.

14. W. M.Wynn, C. P. Frahm, P. J. Carroll, R. H. Clark, J.Wellhoner, and M. J. Wynn, "Advanced superconducting gradiometer/magnetometer arrays and a novel signal

processing technique," *IEEE Trans. Magn.*, vol. MAG-11, no. 2, pp. 701–707, Mar. 1975.
15. F. H. Raab, E. B. Blood, T. O. Steiner, and H. R. Jones, "Magnetic position and orientation tracking system," *IEEE Trans. Aerosp. Electron. Syst.*, vol. AES-15, no. 5, pp. 709–718, Sep. 1979.
16. J. E. Mcfee and Y. Das, "Determination of the parameters of a dipole by measurement of its magnetic field," *IEEE Trans. Antennas Propag.*, vol. AP-29, no. 2, pp. 282–287, Mar. 1981.
17. J. A. Paradiso, K. Hsiao, J. Stricken, J. Lifton, and A. Adler*, IBM Syst.J.*, vol. 39, no. 3 and 4, pp. 892–914, 2000.
18. S. Yabukami, S. Hashi, Y. Tokunaga, T. Kohno, K. I. Arai, and Y. Okazaki, "Development of a position-sensing system for a wireless magnetic marker," *J. Magn. Soc. Jpn.*, vol. 28, pp. 877–885, 2004.
19. S. Hashi, Y. Tokunaga, S. Yabukami, M. Toyoda, K. Ishiyama, Y. Okazaki, and K. I. Arai, "Development of real-time and highly accurate wireless motion capture system utilizing soft magnetic core," *IEEETrans. Magn.*, vol. 41, no. 10, pp. 4191–4193, Oct. 2005.
20. S. Hashi, S. Yabukami, M. Toyoda, M. Ohya, K. Ishiyama, Y. Okazaki, and K. I. Arai, "Magnetic motion capture system using LC resonant magnetic marker composed of Ni-Zn ferrite core," *J. Appl. Phys.*, vol.99, p. 08B312, 2006.
21. M. Toyoda, S. Hashi, S. Yabukami, M. Ohya, K. Ishiyama, Y. Okazaki, and K. I. Arai, "Development of wireless magnetic multi-position detecting system using FFT analysis," *J. Magn. Soc. Jpn.*, vol. 30, pp.391–395, 2006.
22. S. Hashi, M. Toyoda, S. Yabukami, K. Ishiyama, Y. Okazaki, and K. I. Arai, "Wireless magnetic motion capture system for multi-marker detection," *IEEE Trans. Magn.*, vol. 42, no. 10, pp. 3279–3281, Oct. 2006.
23. T. Nakagawa and Y. Koyanagi*, Experimental Data Analysis by the Least Square Method*. Tokyo, Japan: The University of Tokyo Press, 1982, pp. 95–99.
24. F. Shubitidze, B. Barrowes, I. Shamatavaa, J. P. Fernández, and K. O'Neil; "Underwater UXO Detection and Discrimination: Understanding EMI Scattering Phenomena in a Conducting Environment", Defense and security 2008: Homeland Security, Law Enforcement, and Battle space Technologies, 17-20 March, 2008, Orlando Florida, Volume 6953, pp. 69530m-1 69530m-11.
25. Dennis, Jr., J. E., and Schnabel, R. B., [*Numerical Methods for Unconstrained Optimization and Nonlinear Equations*], Prentice-Hall, Englewood Cliffs, New Jersey, 1983.
26. Levenberg, K., "A method for the solution of certain problems in least squares," *Quarterly Journal of Applied Mathematics*, vol. 2, pp. 164–168, 1944.
27. Marquardt, D., "An algorithm for least-squares estimation of nonlinear parameters," *SIAM Journal on Applied Mathematics*, vol. 11, pp. 431–441, 1963.
28. Storn, R., and Price, K., "Differential evolution: a simple and efficient adaptive s*cheme for global optimization over* continuous spaces," *Journal of Global Optimization*, vol. 11, pp. 341–359, 1997.
29. Storn, R., "System design by constant adaptation and differential evolution," *IEEE Trans. Evol. Comput., vol. 3, pp. 2*2–34, 1999.

Technical *publications produced under* this project:

F. Shubitidze, A. Bijamov, Irma Shamatava, John Miller, G. Schultz, Investigating magnetic-field sensor configurations for underwater geo-location." Proc. SPIE **2011,** Orlando, Florida, April 25-29.

F. Shubitidze, Irma Shamatava, John Miller, G. Schultz, "A low frequency magentic field sensor for underwater geo-location." Partners in Environmental Technology Technical Symposium and Workshop, Washington DC, November 30–December 2, 2010..